

The Milky Way's bar and bulge revealed by APOGEE and *Gaia* EDR3

A. B. A. Queiroz^{1,2}, C. Chiappini^{1,2}, A. Perez-Villegas^{3,4}, A. Khalatyan¹, F. Anders^{5,2}, B. Barbuy³, B. X. Santiago^{6,2}, M. Steinmetz¹, K. Cunha^{7,8}, M. Schultheis⁹, S. R. Majewski¹⁰, I. Minchev¹, D. Minniti¹¹, R. L. Beaton¹², R. E. Cohen¹³, L. N. da Costa², J. G. Fernández-Trincado^{14,15}, D. A. García-Hernández^{16,17}, D. Geisler^{13,18,19}, S. Hasselquist^{20,21}, R. R. Lane¹⁴, C. Nitschelm²², A. Rojas-Arriagada¹¹, A. Roman-Lopes¹⁹, V. Smith²³, G. Zasowski²⁰

(Affiliations can be found after the references)

Received June 4, 2022; accepted xx.yy.20zz

ABSTRACT

We investigate the inner regions of the Milky Way using data from APOGEE and *Gaia* EDR3. Our inner Galactic sample has more than 26 500 stars within $|X_{\text{Gal}}| < 5$ kpc, $|Y_{\text{Gal}}| < 3.5$ kpc, $|Z_{\text{Gal}}| < 1$ kpc, and we also make the analysis for a foreground-cleaned sub-sample of 8 000 stars more representative of the bulge-bar populations. These samples allow us to build chemo-dynamical maps of the stellar populations with vastly improved detail. The inner Galaxy shows an apparent chemical bimodality in key abundance ratios $[\alpha/\text{Fe}]$, $[\text{C}/\text{N}]$, and $[\text{Mn}/\text{O}]$, probing different enrichment timescales, which suggests a star formation gap (quenching) between the high- and low- α populations. For the first time, we can, via joint analysis of the distributions of kinematics, metallicities, mean orbital radius and chemical abundances, characterize the different populations coexisting in the innermost regions of the Galaxy. The chemo-kinematic data dissected on an eccentricity- $|Z|_{\text{max}}$ plane reveals the chemical and kinematic signatures of the bar, of a thin inner disk, of a inner thick disk, and a broad metallicity population, with large velocity dispersion, indicative of a pressure supported component. The interplay of these different populations are mapped onto the different metallicity distributions seen in the eccentricity- $|Z|_{\text{max}}$ diagram, consistently with the mean orbital radius and V_{ϕ} distributions. A clear metallicity gradient as a function of $|Z|_{\text{max}}$ is also found, which is consistent with the spatial overlapping of different populations. Additionally, we find and characterize chemically and kinematically a group of counter-rotating stars, which could be the result of gas-rich merger event or just the result of clumpy star formation during the earliest phases of the early disk, which migrated into the bulge. Finally, based on the 6D information we assign stars a probability value of being on a bar orbit and find that most of the stars with large bar orbit probabilities come from the innermost 3 kpc, with a broad dispersion of metallicity. Even stars with high probability of belonging to the bar show the chemical bimodality in the $[\alpha/\text{Fe}]$ vs. $[\text{Fe}/\text{H}]$ diagram. This suggests bar trapping to be an efficient mechanism, explaining why stars on bar orbits do not show a significant distinct chemical abundance ratio signature.

Key words. Stars: abundances – fundamental parameters – statistics; Galaxy: center – general – stellar content

1. Introduction

The Milky Way bulge region, originally identified as a distinct Galactic component by Baade (1946) and Stebbins & Whitford (1947), has traditionally been very challenging to observe, because it is a crowded and extincted region (see Madore 2016 for a review). Photometric studies of the Galactic bulge towards low extinction windows have suggested the region to be essentially old (e.g., Zoccali et al. 2003; Renzini et al. 2018; Surot et al. 2019; Bernard et al. 2018). A spectroscopic sample of bulge lensed dwarfs has indicated a significant population younger than 5 Gyr (Bensby et al. 2017). Optical spectroscopic surveys of the Milky Way traditionally avoid low Galactic latitudes ($|b| \leq 5$ -10) due to the high levels of extinction, especially towards the inner regions. Gonzalez et al. (2013) used the VISTA Variables in the Via Lactea survey (VVV Minniti et al. 2010) to map the mean metallicity throughout the bulge using near-IR photometry, suggesting the existence of a gradient, with the most metal-rich populations concentrated to the innermost regions (Minniti et al. 1995).

Defining a complete sample of the stellar populations in the inner Galaxy has been a challenge. Available spectroscopic samples have been traditionally very patchy and fragmented, especially toward the Galactic bulge where heavy extinction and crowding, make this area hard to observe. Therefore, most of the spectroscopic data of the Milky Way bulge and bar were lim-

ited to a few low-extinction windows (e.g., Baade's Window), or slightly larger latitudes.

Since the pioneer works of Rich (1988) and Minniti et al. (1992), the bulge region has been explored by several spectroscopic surveys, such as BRAVA (Rich et al. 2007; Kunder et al. 2012), ARGOS (Ness 2012), GIBS (Zoccali et al. 2014), GES (e.g., Rojas-Arriagada et al. 2014, 2017), as well as other smaller samples towards lower extinction windows (see Barbuy et al. 2018, for a review that summarises our knowledge on the Galactic bulge up to 2018).

The bulge region was confirmed to be dominated by α -enhanced stars (McWilliam & Rich 1994; Cunha & Smith 2006; Fulbright et al. 2007; Friaça & Barbuy 2017), to have a broad metallicity distribution function (Rich 1988; Gonzalez et al. 2015; Ness & Freeman 2016), to show cylindrical rotation, which is especially contributed by the more metal-rich stars, and to have an X-shape structure which is the result of a buckling bar (e.g., Nataf et al. 2010; McWilliam & Zoccali 2010; Saito et al. 2012; Li & Shen 2012; Wegg et al. 2017). It has also been shown that the oldest bulge populations traced by RR Lyrae or very metal-poor stars do not follow the cylindrical rotation (Dékány et al. 2013; Gran et al. 2015; Kunder et al. 2016, 2020; Arentsen et al. 2020). A mix of stellar populations is detected in the Galactic bulge inferred via the multi-peaked metallicity distribution function (Zoccali et al. 2008; Johnson et al. 2013; Ness et al. 2013b), usually associated with different kinematics (Hill et al.

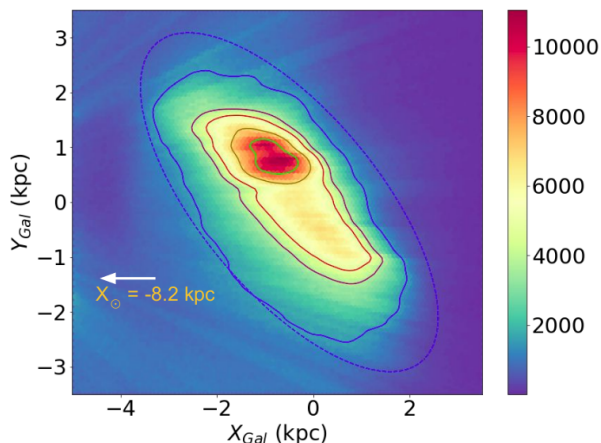


Fig. 1. A magnified view of the Gaia DR2-derived map of the Galactic bar (Anders et al. 2019). The contours represent the four highest density levels. To guide the eye, an ellipse inclined by 45 deg is drawn in blue. Only red-clump stars with good StarHorse flags close to the Galactic plane ($|Z_{\text{Gal}}| < 3$ kpc) are shown. The figure contains *circa* 30 million stars.

2011; Babusiaux et al. 2010, 2014), for a review see Babusiaux (2016); Barbuy et al. (2018). It has been suggested that the Galactic bulge harbours a more spheroidal, but still barred, metal poor (with $[\text{Fe}/\text{H}] \sim -0.5$) component formed by alpha-enhanced stars, and a more metal-rich ($[\text{Fe}/\text{H}] \sim 0.3$) component that forms a boxy bar (Rojas-Arriagada et al. 2014; Zoccali et al. 2017), which can split into more components closer to the midplane (see Table 2 of Barbuy et al. 2018, for a summary).

In the last two years the Galactic Archaeology field was transformed. Firstly, by the advent of the second and third early data release of *Gaia* (DR2, EDR3 Gaia Collaboration et al. 2018, 2020). Secondly, by the near-infrared survey (*H*-band) Apache Point Observatory Galactic Evolution Experiment (APOGEE-2 Majewski et al. 2017; Abolfathi et al. 2018) which has currently been extended to the Southern Hemisphere (Ahumada et al. 2020). It finally became possible to probe the innermost regions of the Galaxy, much closer to the Galactic plane, with expanded samples of stars with full 6D phase-space information and detailed chemistry. This has opened the possibility for much more detailed studies of the innermost Galactic regions, extending the mapping of the mix of stellar populations to orbital-chemical space (i.e. García Pérez et al. 2018; Zasowski et al. 2019; Fernández-Trincado et al. 2019b; Rojas-Arriagada et al. 2019; Sanders et al. 2019a; Queiroz et al. 2020).

The latest *Gaia* dataset enables the Galactic community to tackle several outstanding questions, such as the shape and kinematics of the Galactic halo (e.g., Helmi et al. 2018; Iorio & Belokurov 2019; Myeong et al. 2019), structures in the outer disc (Laporte et al. 2020), the Galactic warp (e.g., Romero-Gómez et al. 2019; Poggio et al. 2020; Cheng in prep.), recently the disk spiral structure (Poggio et al. 2021) and also the effect of bar resonances (Kawata et al. 2020). In Anders et al. (2019), we used the Bayesian StarHorse code (Queiroz et al. 2018; Santiago et al. 2016) to derive photo-astrometric distances and extinctions for around 265 million *Gaia* DR2 stars down to magnitude $G < 18$. Our calculations allowed for the first time a direct detection of the Galactic bar from *Gaia* data, from the stellar density maps. Figure 1 shows a zoomed-in version of the red-clump density map presented in Anders et al. (see 2019, their fig. 8). The breathtaking amount of data (almost 30 million stars with accurate distances and extinctions) shows the clear shape of an elongated structure around the Galactic centre, associated

with the Galactic bar. The map of Figure 1 shows the stellar density contours and an ellipse tilted by 45 deg with respect to the Sun-Galactocentric line, adjusted by eye. This bar orientation is considerably larger than the ~ 30 degrees inferred by most other works (e.g., Wegg & Gerhard 2013; Cao et al. 2013; Rattenbury et al. 2007; Minchev et al. 2007; Sanders et al. 2019b), but in the range of predictions from modeling of the solar neighborhood velocity field (e.g., Dehnen 2000; Minchev et al. 2010). The higher density towards positive Y values is an effect of the lower extinction in that area.

Although a very clear image of the bar can be seen, the StarHorse catalogue of Anders et al. (2019) contains some caveats that render a profound exploration and characterization of the bulge-bar population difficult. Firstly, the map was derived from parallaxes and photometry only, both of which have elevated uncertainties for the Galactic central region. Secondly, for this sample StarHorse was run with a fixed range of possible extinction values ($A_V < 4$ mag), which is not a problem for most regions of the Galaxy, but in the central Galactic plane the extinction can be much higher than 4 mag (e.g., Gonzalez et al. 2012; Queiroz et al. 2020). To further characterise the bulge-bar populations we need large samples of stars observed with infrared spectroscopy, which is now becoming possible with APOGEE DR16.

In this work we use data from APOGEE which provides spectra for thousands of stars also at low latitudes, where most of the Milky Way stellar mass is concentrated. The main challenge has been the determination of precise distances to better define bulge samples to constrain, in turn, chemodynamical models. Thanks to the availability and improvements of *Gaia* EDR3 parallaxes in the APOGEE footprint, we derived precise distances and extinctions for the APOGEE stars using the StarHorse code (Queiroz et al. 2020), achieving individual distance uncertainties of typically 10% toward the Galactic centre (see also Schultheis et al. 2019). This makes it finally possible to attempt to disentangle the complex mixture of stellar populations coexisting in the inner Galaxy, which is the goal of the present work.

Although the analysis presented in this paper is based on two samples much smaller than the one shown in Figure 1, the rich information provided by combining *Gaia* EDR3 and APOGEE allows an unprecedented view of the innermost regions of the Milky Way and first complete analysis of the sample in the orbital space. We are now in a position to offer much tighter observational constraints to chemodynamical simulations of the bulge-bar, contributing to clarify the current debate as to whether the Galactic bulge has a dispersion-dominated component resulting from mergers and/or dissipative collapse of gas (Minniti et al. 1992; Zoccali et al. 2008), or if its properties can be completely accounted for by secular dynamical processes forming a buckling bar from pure disk evolution (Debattista et al. 2017; Buck et al. 2019; Fragkoudi et al. 2020). So far, the broad range of available observational signatures seem to suggest a hybrid scenario, in which the metal-poor and the metal-rich populations present in the bulge region, would accommodate both the dispersion-dominated and secular-dominated scenarios, respectively (see also discussion in Section 4 of Barbuy et al. 2018). Recent results and discussions based on different kinematical populations of RR Lyrae (Kunder et al. 2020) also found evidence for bimodal distributions, as well as a small fraction of metal-poor stars and bulge globular clusters - see Fernández-Trincado et al. 2020b.

The paper is organised as follows. In Section 2 we describe the spectroscopic data. Section 3 describes the computation of velocities and orbital parameters. In Section 4 we describe our sample selection which consists of an inner-region sample (of

around 26 500 stars) and more inner sample, avoiding the foreground disk (with around 8 000 stars). The chemical and dynamical properties of both samples are described in Section 5 (with particular focus on the observed chemical bimodality), and in Section 6. In Section 7 we dissect the sample into families in the eccentricity- $|Z|_{\max}$ plane. The results and their implications are summarised and discussed in Section 8.

2. Data

The APOGEE survey is building a detailed chemo-dynamical map extending over all components of the Milky Way. Being the first large spectroscopic survey to explicitly target the central Galactic plane (Zasowski et al. 2013, 2017), thanks to its near-infrared spectral range (1.5 - 1.7 μm ; *H*-band), APOGEE allows us to determine precise line-of-sight velocities, atmospheric parameters, and chemical abundances, even in highly extincted areas. APOGEE started as one of the Sloan Digital Sky Survey III (Eisenstein et al. 2011, SDSS-III) programs and is continuing as part of SDSS-IV (Blanton et al. 2017). The observations started in 2011 at the SDSS telescope (Gunn et al. 2006) with the northern high-resolution, high signal-to-noise ($R \sim 22\,500$, $S/N > 100$) APOGEE spectrograph (Wilson et al. 2010). Since 2017, southern observations have been conducted with a twin spectrograph mounted at the du Pont telescope at Las Campanas Observatory (Wilson et al. 2019).

The latest release of APOGEE data, SDSS DR16 (Ahumada et al. 2020), includes observations from the Southern Hemisphere and contains spectral observation for about 450 000 sources. Given the DR16 sky coverage and high-quality observations in the Galactic plane, we can study the Galactic bulge and bar both in the chemical and dynamical space with unprecedented completeness. Besides the data from APOGEE DR16 we also use the incremental DR16 internal data release which has about + 150 000 additional stars observed through March 2020. Spectral information is obtained through the APOGEE Stellar Parameters and Chemical Abundances Pipeline (ASPCAP García Pérez et al. 2016; Jönsson et al. 2020). This pipeline compares the observations with a large library of synthetic spectra, determining a best chi-squared fit. The first step in the process is to derive stellar atmospheric parameters and overall abundances of C, N, alpha-elements. Then, the second step is to derive abundances from fits to windows tuned for each atomic element. Throughout this paper we use $[M/H]$ (obtained in the first step in ASPCAP) as our metallicity. The studied elements in this paper are: $[\alpha/\text{Fe}]$, $[\text{Fe}/\text{H}]$, $[\text{O}/\text{Fe}]$, $[\text{Mg}/\text{Fe}]$, $[\text{Mn}/\text{O}]$, $[\text{Mn}/\text{Fe}]$, $[\text{C}/\text{N}]$ and, $[\text{Al}/\text{Fe}]$. The APOGEE internal released data has a slightly updated data reduction version (r13). From the APOGEE catalogue, we select only stars with high signal to noise, $\text{SNREV} > 50$, and a good spectral fit from the ASPCAP pipeline, $\text{ASPCAP_CHI2} < 25$. Besides the APOGEE data, to define a bulge-bar sample we need precise distance measurements. To this end we use *StarHorse* (Santiago et al. 2016; Queiroz et al. 2018) - a Bayesian tool capable of deriving distances, extinctions and other astrophysical parameters based on spectroscopic, astrometric, and photometric information. In Queiroz et al. (2020) we combined APOGEE DR16 spectroscopy with *Gaia* DR2 parallaxes corrected for a systematic -0.05 mas shift (Gaia Collaboration et al. 2018; Arenou et al. 2018; Zinn et al. 2019), photometry from 2MASS (Cutri et al. 2003), PanSTARRS-1 (Chambers et al. 2016), and AllWISE (Cutri et al. 2013) to produce spectro-photometric distances, extinctions, effective temperatures, masses and surface gravities for around 388 000 stars. In that paper, we also make the same calculation for other major spectroscopic surveys summing a total of 6 million stars with re-

sulting *StarHorse* parameters.

For the data used throughout this paper, we follow the same procedure as in Queiroz et al. (2020) and run *StarHorse* for the APOGEE DR16 internal release + *Gaia* EDR3 parallaxes and the same set of photometry. Corrections were applied to parallaxes as recommended by Lindegren et al. (2020). With *Gaia* EDR3, the resulting distance errors are greatly improved. The samples used along this work have distance uncertainties around 7%, while previous computations using *Gaia* DR2 allowed us uncertainties compared around 10%. However the main difference is the improvement on proper motions as we will discuss in the next section.

3. Velocities and orbits

The combined catalogue APOGEE DR16 internal release + *Gaia* EDR3 + *StarHorse* gives us access to the 6D phase space of the stars with unprecedented precision. We use the *Gaia* EDR3 proper motions, the line-of-sight velocities (V_{los}) measured by APOGEE and the *StarHorse* distances to calculate the space velocities in Galactocentric cylindrical coordinates. The cylindrical velocity transformations were performed using *Astropy* library coordinates (Price-Whelan et al. 2018), where we use a Local Standard of Rest of $v_{\text{LSR}} = 241$ km/s (Reid et al. 2014), the distance of the Sun to the Galactic centre of $R_{\odot} = 8.2$ kpc, and height of the Sun from the Galactic plane of $Z_{\odot} = 0.0208$ kpc (Bennett & Bovy 2019). Notice also, in all of our diagrams we use the Sun position at $X_{\text{Gal}} = -8.2$ kpc.

We assume the peculiar motion of the Sun with respect to the LSR to be: $(U, V, W)_{\odot} = (11.1, 12.24, 7.25)$ km/s (Schönrich et al. 2010). The resulting components of the velocity we use throughout this paper are the azimuthal velocity, V_{ϕ} , the radial velocity V_R , and the vertical velocity V_Z . All these components are with respect to the GC. Notice that $V_R \neq V_{\text{los}}$.

Since all bodies in the Milky Way move under the Galactic potential, many stars that we find nowadays with a present position at the Galactic center may actually be in a disc or halo orbits. To identify if the stars are from disc, halo or from bulge-bar components we proceed with the calculation of the orbital parameters. Our Galactic potential includes an exponential disk generated by the superposition of three Miyamoto-Nagai discs (Miyamoto & Nagai 1975; Smith et al. 2015), a dark matter halo modeled with an NFW density profile (Navarro et al. 1997), and a triaxial Ferrers bar (Ferrers 1877; Pfenniger 1984). The total bar mass is $1.2 \cdot 10^{10} M_{\odot}$, the angle between the bar's major axis and the Sun-Galactocentric line is 25 deg, its pattern speed is 40 $\text{km s}^{-1} \text{kpc}^{-1}$ (Portail et al. 2017; Pérez-Villegas et al. 2017b; Sanders et al. 2019a) and its half-length is 3.5 kpc. To consider the effect of the uncertainties associated with the observational data, we used a Monte Carlo method to generate 50 initial conditions for each star, taking into account the errors of distances, heliocentric line-of-sight velocities, and the absolute proper motion in both components. We integrate those initial conditions forward for 3 Gyr with the NIGO tool (Rossi 2015). From the Monte Carlo experiment, we calculated the median of the orbital parameters for each star: perigalactic distance R_{peri} , apogalactic distance R_{apo} , the maximum vertical excursion from the Galactic plane $|Z|_{\max}$, the eccentricity $e = (R_{\text{apo}} - R_{\text{peri}})/(R_{\text{apo}} + R_{\text{peri}})$ and the mean orbital radius, $R_{\text{mean}} = (R_{\text{apo}} + R_{\text{peri}})/2$. In the next sections we will use those orbital parameters when analysing the chemical patterns found in the innermost regions of the Galaxy. We show the uncertainties in the orbital parameters and cylindrical velocities in Figure 2. These distributions increase with increasing distance, which is expected since for larger distances

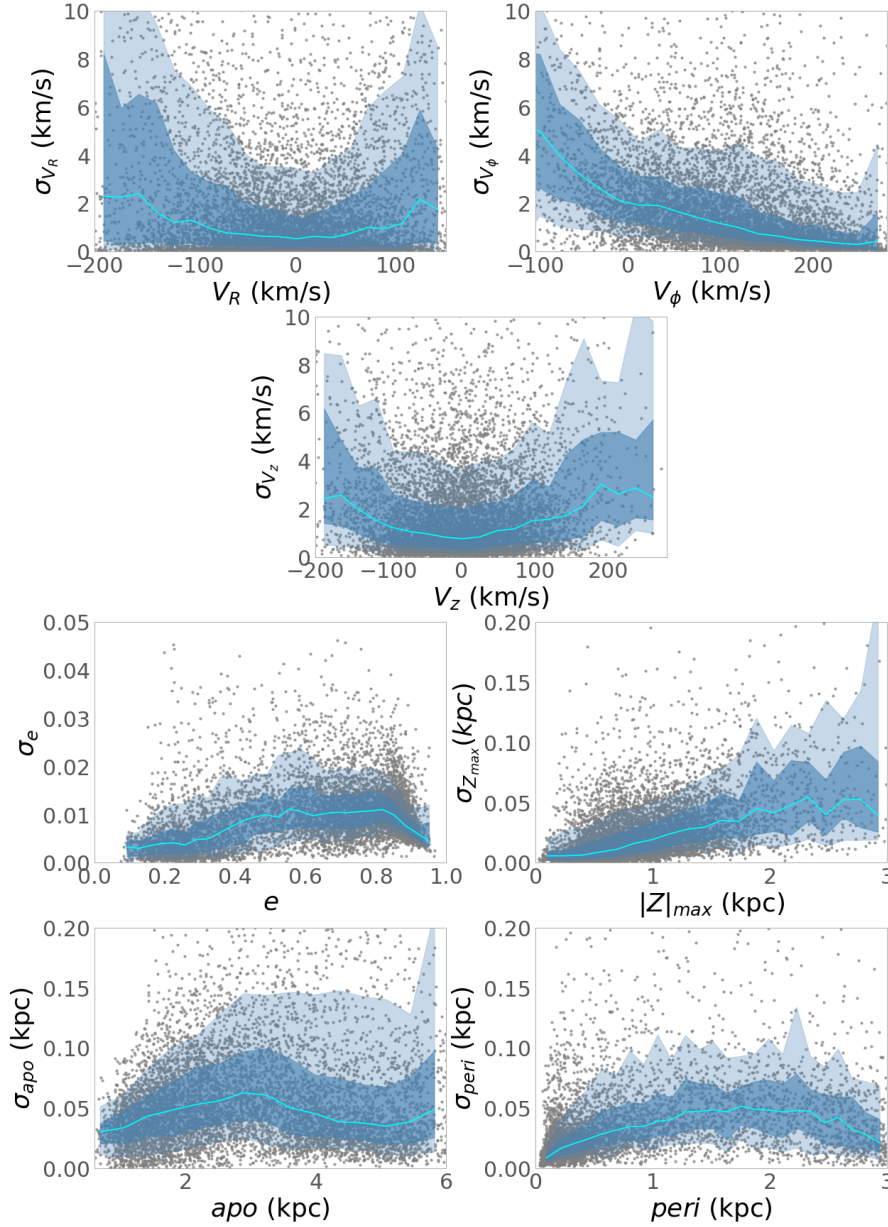


Fig. 2. Standard error of the cylindrical velocities and orbital parameters. The blue line and shaded areas show the distribution’s median and standard deviation of 1σ and 2σ .

we have larger *StarHorse* distance uncertainties. The uncertainties in velocity are larger for retrograde stars (negative v_ϕ) but still usually around 5 km/s. The other components of the velocity show higher uncertainties for faster stars.

One caveat in these calculations is the fact that orbital parameters depend on the model employed. We integrated the orbits in a steady-state gravitational potential. In our model, we do not take into account dynamical friction and the secular evolution of the Galaxy (Hilmi et al. 2020). Also, we do not consider the dynamical effects due to the spiral arms. In Figure B.1 of the Appendix, we show a comparison of the orbital parameters computed using different bar pattern speeds. The comparison gives relative differences smaller than 20% for most of the stars.

4. Sample selection

In this paper we focus our analysis on the inner region of the Milky Way. In particular, we study a window symmetric about the Galactic center in all three dimensions in Galactocen-

tric Cartesian coordinates, shown in Figure 4, ($|X_{\text{Gal}}| < 5$ kpc, $|Y_{\text{Gal}}| < 3.5$ kpc and $|Z_{\text{Gal}}| < 1.0$ kpc).

Throughout the paper, we use two samples: 1). the full bulge-bar sample with the geometric cuts (detailed in Sect. 4.1), and 2). a proper-motion-cleaned subsample (see Sect. 4.2).

The uncertainties in distance and extinction are shown in Figure 3 for the two samples discussed next, the bulge-bar sample and the reduced proper motion sample (RPM). It shows that our stars have uncertainties in distance below 15% which would translate to around 1.5 kpc for the stars with the largest errors. The distribution in distance uncertainties shows no big differences with quality cuts such as parallax relative errors $> 20\%$ or by using only calibrated ASPCAP inputs. The extinction uncertainties from *StarHorse* has three main peaks, $A_V \sim 0.05$ mag, $A_V \sim 0.2$ mag and $A_V \sim 0.3$ caused by the availability or not from one or more passbands from the full photometric set: {2MASS, AllWISE, PanSTARRS-1}. For a further discussion about the uncertainties of these parameters and their correlations please see Queiroz et al. (2018) and Queiroz et al. (2020).

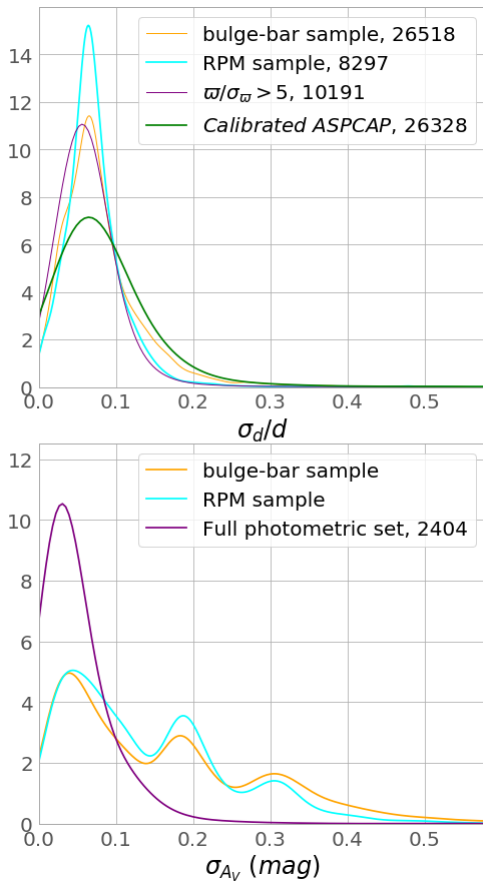


Fig. 3. Upper panel: Distance uncertainty distributions for the bulge-bar (orange) and RPM (cyan) samples defined in Sections 4.1 and 4.2, respectively. Also shown are stars with parallax uncertainties smaller than 20% (magenta) and stars having calibrated ASPCAP parameters (green). Lower panel: Extinction uncertainty distribution for the bulge-bar (orange) and RPM (cyan) samples. Also shown are stars for which all photometric bands are available (magenta). This illustrates that the secondary and tertiary peak at larger extinction uncertainties seen in our samples, are due to stars for which the optical band is not available (see discussion in Queiroz et al. 2020).

4.1. bulge-bar sample

The full bulge-bar sample has a total of 26 518 stars, with typical distance uncertainties around 7% (see below). This APOGEE DR16 inner Galactic sample has unprecedented coverage of thousands of stars that reach Galactic latitudes below $|b| < 5$. This low latitude range was not covered before with previous dedicated surveys such as BRAVA and ARGOS, which were fundamental to reveal the peanut bar shape and to show the rotation of the stars in the Galactic Centre (GC) (Kunder et al. 2012; Ness et al. 2013b). Figure 4 shows in the upper panels Galactocentric density maps in Cartesian (left panel) and cylindrical (right panel) coordinates, and in the lower panels the same projections but colour-coded by our extinction estimates. Figure 4 is by far not as complete in density as Figure 1, however the dense areas in the figure do seem to follow a bar-shaped pattern with higher density around the GC. If we trace again an ellipse by eye around the density contours, we obtain a much smaller inclination angle with respect to the Sun-GC line, of around 20 deg, and thus much closer to the canonical value of ~ 27 deg (Bland-Hawthorn & Gerhard 2016). The fitted ellipse is certainly not precise enough to determine the bar angle, but we clearly see

that the bar shaped structure is less inclined than in Anders et al. (2019).

This seems to confirm the suspicion that the photoastrometric distances for the bar structure seen in Figure 1 may be slightly overestimated because the extinction values get saturated at around $A_V = 4$. Figure 4 also shows that we still lack data very close to the Galactic plane, $|Z_{\text{Gal}}| < 0.2$ kpc, as this area remains hidden by very high extinction, (e.g., for $|Z_{\text{Gal}}| < 0.1$ kpc we often observe large scale extinction $A_V > 10$; Minniti et al. 2014). The Kiel diagram for this sample is shown in the first panel of Figure 5, showing that the population in this sample is composed mainly by red giant branch stars and red clump stars.

4.2. Reduced Proper-motion diagram selection

There are different ways to select a cleaner and more homogeneous bulge-bar sample, avoiding foreground disk stars. Usually studies of bulge stars select fields in the direction of Baade's window (Babusiaux et al. 2010; Hill et al. 2011) or fields in the direction of the Galactic centre (Zoccali et al. 2008; Kunder et al. 2012; Rich et al. 2012). We have in hands a massive set of information about the stars, and besides just selecting the bulge-bar sample we can constrain an even more "clean" sample. One way is to draw iso-contours around the XY density maps. Another way is to look for similarities in the stellar composition. However, we could still be left with disk or halo stars and/or potentially important systematic abundance differences resulting from the fact that stars at different distances will have systematically different luminosities/stellar parameters. Additionally an abundance pre-selection would bias the study towards the chemical distribution of the bar-bulge components.

For our definition of a clean bulge-bar sample, we therefore opt for a selection in the RPM diagram. Our goal with this selection is to clean the most apparent disk contamination without an abrupt cut in distances.

The RPM (Faherty et al. 2009; Gontcharov 2009; Smith et al. 2009) is a common tool used to distinguish between distinct kinematical populations. In the RPM diagram, $M_{H'}$, is defined analogously to the absolute magnitude, since the proper motions are also a proxy for the star's distance:

$$M_{H'} = H_{2\text{mass}} + 5.0 + \log_{10}(\sqrt{\mu_{\text{RA}}^2 + \mu_{\text{DEC}}^2}). \quad (1)$$

In Figure 6 we show the RPM diagram, $(J - K_s)_0$ vs. $M_{H'}$, for the bulge-bar sample defined above. The RPM diagram shows two agglomerations highlighted by the density contour levels, indicating distinct populations and/or corresponding to the possible abundance systematic with effective temperature (e.g., Holtzman et al. 2018). A cut in $|l|, |b| < 10$ (middle panel of Figure 6), is analogous to a cut selecting the rightmost agglomeration as is roughly indicated by the red rectangle, showing this cut represents the innermost population. The left-most agglomeration extends in colour connecting with the right-most stellar overdensity. In our selection, this population's tail remains since we want to preserve completeness and a more symmetrical colour cut around the right-most overdensity. The selection of stars inside the red rectangle also results in the exclusion of most of red clump stars (RC), as one can see in Figure 5. Our goal with this simple selection is to trim disk stars with the fewer biases possible to study chemistry and kinematics. Notice also that the cut in kinematics is minimal, we mostly cut the tails of the proper motion distribution, which have lower density bins. Therefore the RPM cut is more consistent with a colour-cut than a kinematic cut.

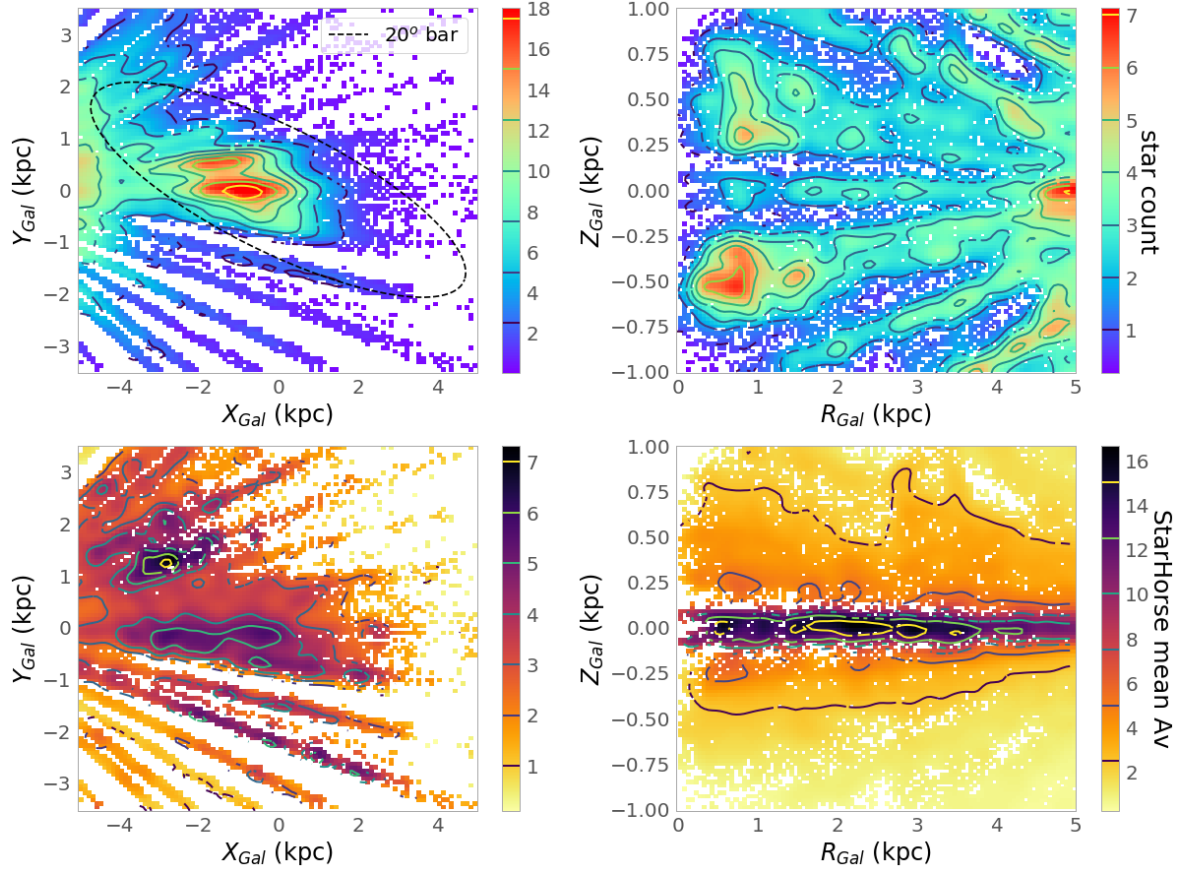


Fig. 4. Cartesian (left panels) and Cylindrical (right panels) projections of the Galactic centre using the APOGEE survey and StarHorse distances. Upper panels show the map colour-coded by the logarithmic number of stars and lower panels colour-coded by StarHorse extinction. Contours are shown for the densest regions as indicated by the colour bar. An ellipse is drawn in the first panel to indicate the approximate location of the Galactic bar.

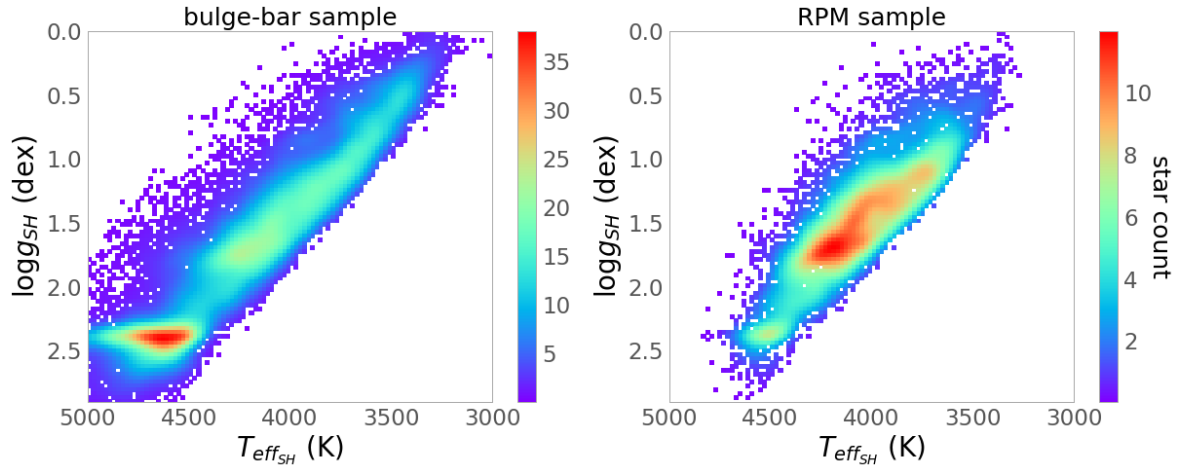


Fig. 5. Kiel diagrams for the complete bulge-bar sample (left) and the RPM selected sample (right). This figure illustrates that the innermost regions of the Galaxy are sampled by the more luminous stars. Because more luminous stars tend to be more metal-poor this bias needs to be considered during the analysis.

With this selection we maintain a relatively homogeneous coverage of the entire inner Galaxy, while removing back- and foreground over-density of disc RC stars. The RPM diagram selection right panel of Figure 6 results in a more smoothly distributed population around the GC and slightly distorts the density contours found for the purely geometric bulge-bar sample. The squared selection was chosen for simplicity, since the main purpose of this stricter sample is to find out whether the results

found with the full sample are robust - or if they may be significantly biased by the complex mix of stellar populations, the selection function of APOGEE, or abundance systematics.

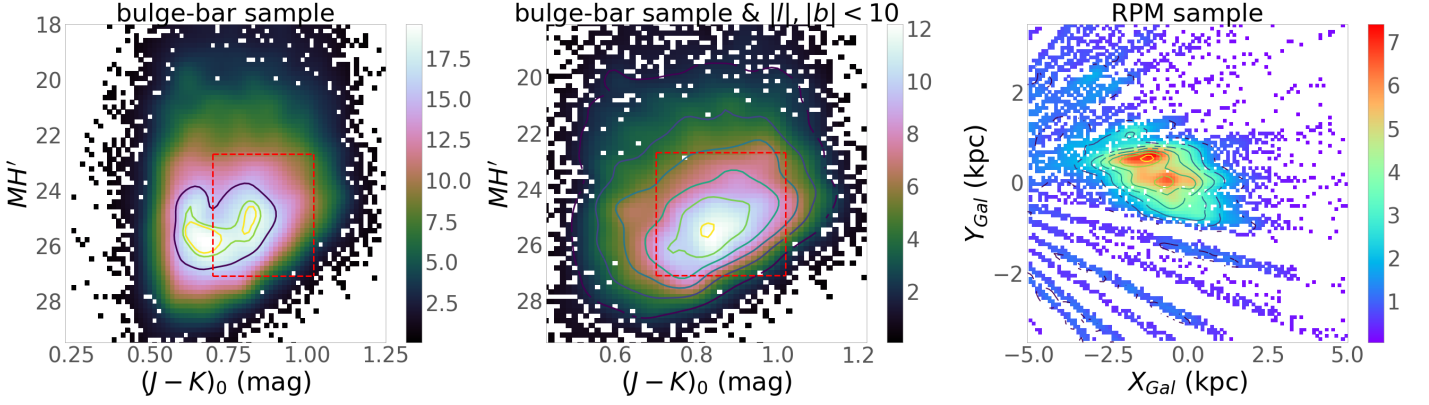


Fig. 6. Illustration of our RPM selection. Left panel: RPM diagram, contours show the most dense areas, highlighting two main density groups. Middle panel: same as left panel, but for the central region ($|l|, |b| < 10$ deg). In both panels, the red dashed box indicates the boundaries of our RPM selection. Right panel: Cartesian density map of stars satisfying the RPM cut.

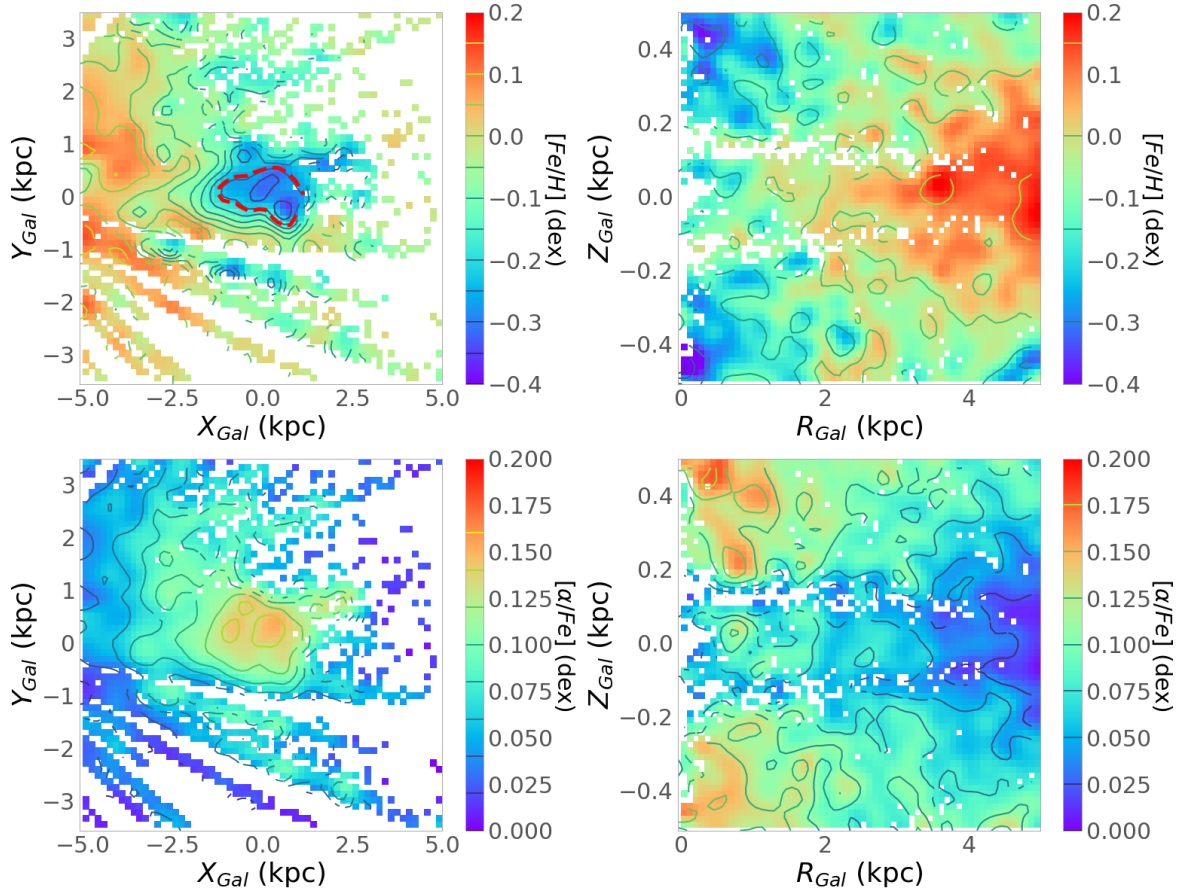


Fig. 7. Cartesian (left panels) and Cylindrical (right panels) Galactocentric projections of the bulge-bar sample with an extra cut of $|Z| < 0.5$ kpc. The Figure is colour-coded by the mean $[Fe/H]$ (upper panels) and $[\alpha/Fe]$ (lower panels) content in each bin. A red contour is drawn around the metal poor area in the innermost regions of the Milky Way.

5. Chemical composition

5.1. The α -elements and metallicity

As mentioned in Section 1, the chemical composition of the bulge-bar region is fairly complex, for example by its multi-peaked metallicity distribution (e.g., Ness et al. 2013b; Rojas-Arriagada et al. 2014, 2017; Schultheis et al. 2017; García Pérez et al. 2018; Rojas-Arriagada et al. 2020), and the fact that the innermost regions of the Milky Way show not only the signature of a bar and a spheroid but also that of the stars from the halo, the thin and the thick disks (Minniti 1996). In particular it is still

debated whether the thin and thick disks might have different chemical signatures in the inner regions than their local counterparts see discussion in (Barbuy et al. 2018; Lian et al. 2020). This is especially the case for the thin disk as shown by the metallicity gradients with Galactic radius (e.g., Hayden et al. 2014; Anders et al. 2014, 2017). Moreover, debris from accreted globular clusters and dwarf galaxies are also expected to populate the central regions of the Milky Way (see Das et al. 2020; Horta et al. 2021; Fernández-Trincado et al. 2019a, 2020a, 2021).

In this section we first focus on the main chemical characteristics of our inner Galactic samples as defined in the previ-

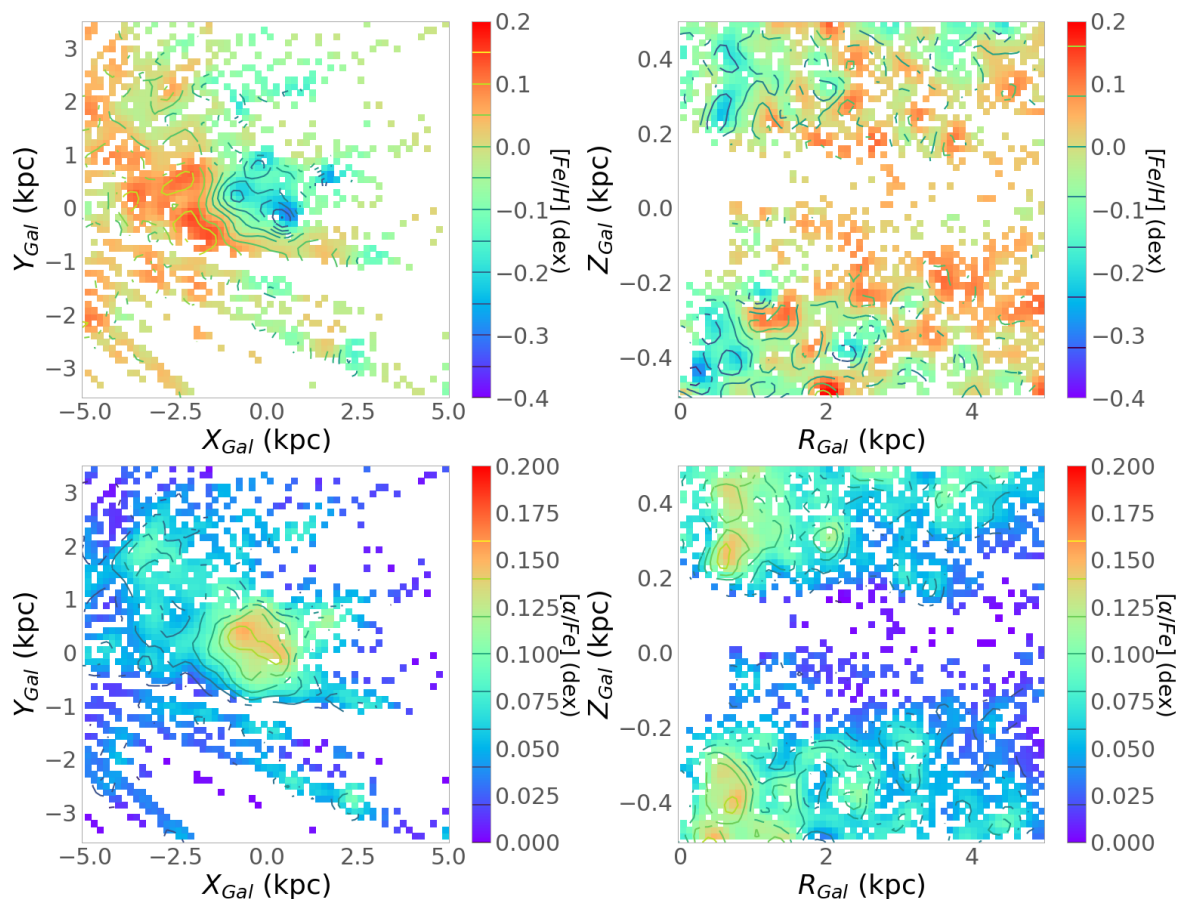


Fig. 8. As Figure 7, but now for the RPM sample, with around 3 800 stars. Notice the lack of stars very close to the midplane, resulting from the fact we do not have *Gaia* proper motions for a considerable fraction of these stars.

ous sections. One important thing to keep in mind is that we have used the ASPCAP $[M/H]$ value as representative of metallicity, as explained in Section 2. No fundamental difference in results is seen between the use of $[Fe/H]$ or $[M/H]$ as the proxy for metallicity, but we retain a larger number of metal-rich, $[M/H] > 0.2$ dex, stars if $[M/H]$ is used (see Section 7.2).

In the present work we have chosen to focus only on the following four abundance ratios: a) the classical $[\alpha/Fe]$ ratio (as well as $[O/Fe]$ and $[Mg/Fe]$ for consistency checks, although for fewer stars), which is available for the whole sample and is a good tracer of the chemical enrichment timescales (e.g., Matteucci 1991; Haywood 2012; Miglio et al. 2021); b) $[C/N]$, which is used in the solar vicinity as a cosmic clock (Masseron & Gilmore 2015; Martig et al. 2016a; Hasselquist et al. 2019); c) the $[Mn/O]$ and $[O/H]$ ratios which also separate thick and thin disk stars (e.g., McWilliam et al. 2013; Barbuy et al. 2013, 2018).

Figure 7 shows the spatial chemical abundance maps in Cartesian (XY) and cylindrical (RZ) coordinates colour-coded by $[Fe/H]$ and $[\alpha/Fe]$ abundances for the bulge-bar sample with an extra cut in Galactic height $|Z| < 0.5$ kpc, this sample contains $\sim 14\,500$ stars. The map shows an interesting spatial dependency of the metallicity, with a metal-poor (α -rich) component that seems to dominate the more central region, a feature that we can now see for the first time in the XY plane. Note that selection effects alone would not be able to explain such structure, since such effects would be related to the distance, and we can clearly see the contribution from low metallicity stars increases towards the Galactic centre, $X_{Gal} \sim 0$ kpc, heliocentric distance $d \sim 8$ kpc, and that at greater distances the metallicity starts do in-

crease again (although more data are needed to confirm this point especially in the Galactic southern hemisphere). In photometric samples of the bulge area as a whole, the metal-rich population seems to dominate, as photometric maps report an increase of the metallicity towards the innermost Galactic regions Gonzalez et al. (2013). The more detailed data discussed here enables one to see the spatial variations of the mean metallicity for stars closer to the Galactic midplane ($0.2 < |Z_{Gal}| < 0.5$), showing a clear inversion of the radial metallicity gradient in the innermost 1 kpc. In the Galactic center the metallicity seems to be high again as shown by Schultheis et al. (2019).

The RZ projection also shows large metallicity values (and lower $[Mg/Fe]$) closer to the Galactic midplane, becoming much less prominent at higher latitudes, a result already known from previous studies of the bulge MDF Zoccali et al. (e.g., 2008) inferred in the latitude, longitude space. The projection also shows that the central metal-poor population extends to high Z_{Gal} . In the very low Galactic plane $Z_{Gal} < 0.2$ kpc there is a lack of data due to high extinction (e.g., Minniti et al. 2014; Queiroz et al. 2020), and therefore we are not able with the current sample to determine if the innermost population is dominated by metal-rich or metal-poor stars.

It is beyond the scope of this paper to correct for selection effects, which we plan to do in a future work specifically dedicated to the detailed comparison of our data with chemo-dynamical models. In the case of APOGEE the lines of sight and magnitude determine the selection function, which can limit the populations in age or chemistry. In an upcoming paper (Queiroz et al., in prep.) we will use mock simulations to study how these selection effects affect our sample. However, the selection func-

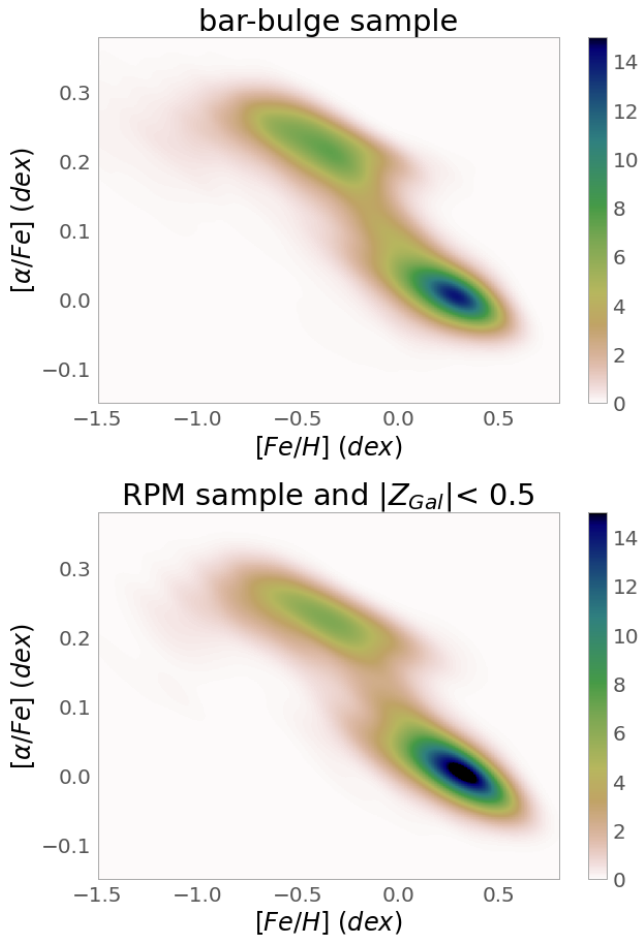


Fig. 9. $[\alpha/\text{Fe}]$ vs. $[\text{Fe}/\text{H}]$ distributions for the bulge-bar region ($\sim 26\,500$ stars), and RPM sample ($\sim 3\,800$ stars with $|Z_{\text{Gal}}| < 0.5$ kpc), colour-coded by the probability density function.

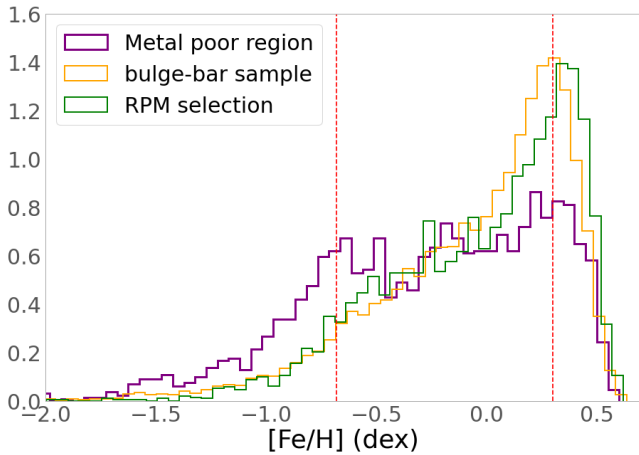


Fig. 10. Metallicity distribution function for the bulge-bar field, RPM sample and metal poor region highlighted in Figure 7. The prominent peaks of the distributions are indicated by the vertical dashed lines

tion seems to have a minor impact, as illustrated by other recent work of Rojas-Arriagada et al. (2020) using APOGEE DR16, and also by work using DR14 Nandakumar et al. (2017). A bias towards preferentially observing metal-poor (brighter) objects in the most reddened regions seems to exist. Here we try to gauge this effect by investigating the RPM sample, which is shown in Figure 8. This figure shows a considerable lack of data in the

most central regions of the Galaxy at $Z_{\text{Gal}} < 0.2$ kpc compared to the bulge-bar sample. The absence of data in the low Galactic plane in the RPM sample results from the *Gaia* EDR3 unavailability in the high extinction and crowded areas such as the inner Galaxy. From the bulge-bar sample, around $\sim 3\,000$ stars have no *Gaia* EDR3 proper motions. Those are almost all located at low Galactic heights. Given this fact, there is no apparent shift to more metal-poor stars in the central regions sampled by the RPM selection than as is seen when analyzing the bulge-bar sample. Notice that in the inner 200 pc regions, and in particular close to SgrA within the Nuclear Star Cluster, one finds a very metal-rich dominant population (Schultheis et al. 2019). In any case, these caveats should be kept in mind when discussing the results that relate chemistry with kinematics and orbital parameters in Sections 6 and 7, especially in the lower Z_{Gal} regions, and when extracting conclusions from 2-D chemical abundance diagrams.

The $[\alpha/\text{Fe}]$ vs. $[\text{Fe}/\text{H}]$ plane is now shown for our two samples in Figure 9. In the figure we use kernel density estimation from *scipy* (Virtanen et al. 2019) to estimate the probability density function. In both cases, the sequences show a bimodal distribution with an α -rich and α -poor populations, with the two sub-components becoming better defined when we apply the proper motion selection to clean for foreground stars, and confine the sample to near the Galactic midplane. This bimodality has also been reported by Rojas-Arriagada et al. (2019) using APOGEE DR14 data, though both in the paper by Queiroz et al. (2020) and here the depression between the two peaks is significantly clearer, with the two sequences markedly separated. The metallicity distribution of our two samples is shown in Figure 10. The Galactic bulge has long been reported to have multiple peak locations in the metallicity distribution (McWilliam 1997), but the peak metallicity values vary considerably according to the sample and technique used, (see Table 2 of Barbuy et al. 2018). From Figure 7, we select all the stars that fall within the highlighted red-dashed contour line in the upper left panel, and we plot the resulting metallicity distribution in Figure 10. This region of stars has at least two peaks in the metallicity distribution: the most dominant peak at $[\text{Fe}/\text{H}] = 0.30$ and intermediate peak at $[\text{Fe}/\text{H}] = -0.68$. This is in agreement with the peaks found by Rojas-Arriagada et al. (2020) -0.66 , -0.17 and $+0.32$ dex, respectively. The multi-peaked metallicity distribution seen here can also be associated with different stellar populations in the Galactic bulge, as in Ness et al. (2013a). However, there is no requirement for a physically motivated population to have a Gaussian or narrow chemical composition. For a detailed study of the APOGEE DR16 MDF as a function of (l, b) we refer to Rojas-Arriagada et al. (2020). The MDF of our samples will be discussed in Section 7 in the context of the chemo-orbital analysis. Finally, we have also looked at two individual α -elements, O and Mg, to ensure we obtain consistent results with what is found using the α values obtained from the ASPCAP pipeline. Figure 11 shows the $[\text{O}/\text{Fe}]$ (with 13 421 stars) and $[\text{Mg}/\text{Fe}]$ (with 13 473 stars) maps for the bulge-bar field sample. The results are consistent with the maps shown in Figure 7. In Figure 13, which is similar to Figure 9 but made using $[\text{O}/\text{Fe}]$ and $[\text{Mg}/\text{Fe}]$, and only for the RPM sample, the bimodality is still visible, though with a different morphology when Mg is used. The different morphologies are in part most probably a consequence of details on the stellar pipelines. The APOGEE/ASPCAP dispersion in uncertainties for $[\text{Mg}/\text{Fe}]$ is higher for colder low/intermediate metallicity stars (Jönsson et al. 2020).

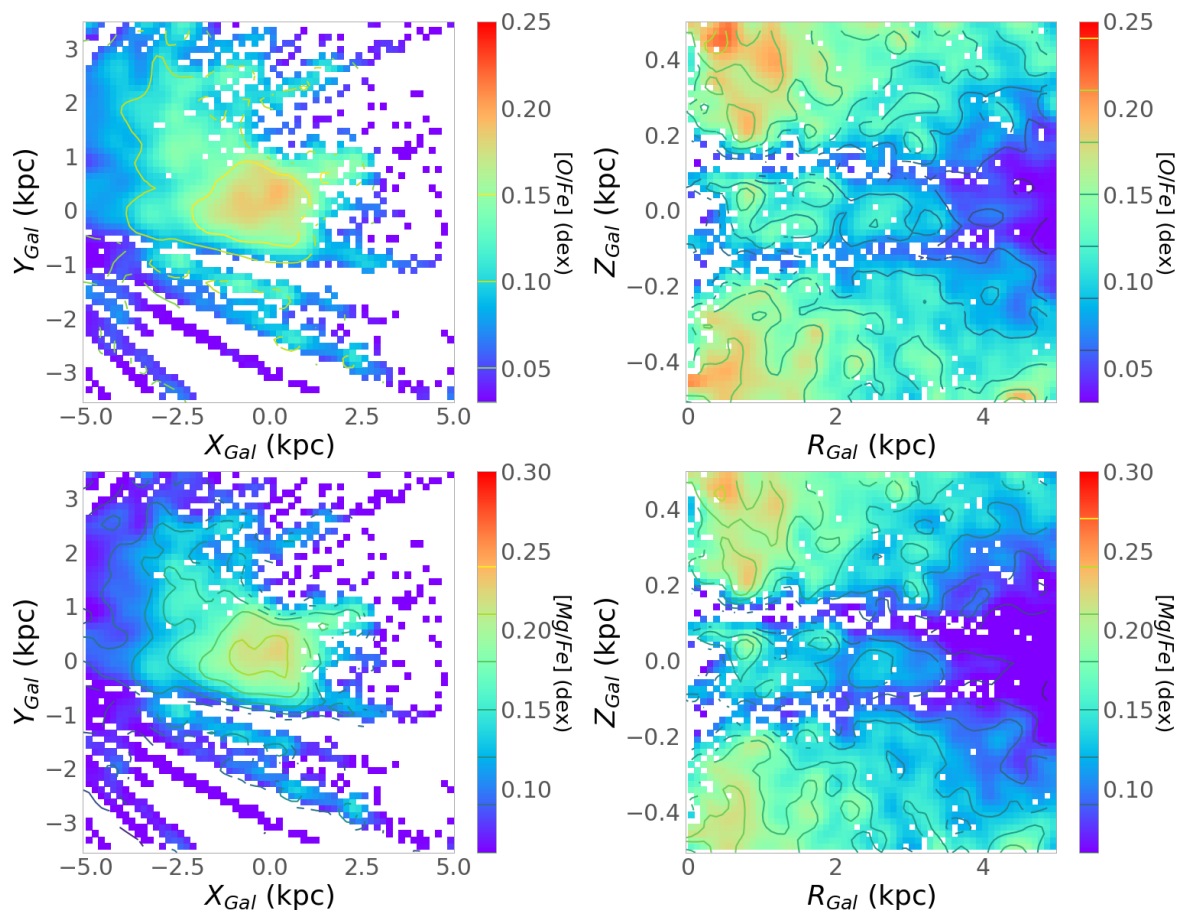


Fig. 11. Same as Figure 7 but now colour-coded by the mean in $[O/Fe]$ (upper panels) and $[Mg/Fe]$ (lower panels) content per bin. These maps are fully consistent with what was seen before when using the ASPCAP α instead of the individual alpha elements given by the pipeline.

5.2. Checking for consistency with two other chemical clocks: $[C/N]$ and $[Mn/O]$

Other important chemical clocks are the $[C/N]$ and $[Mn/O]$ abundance ratios. The $[C/N]$ is broadly dependent on the stellar mass, since the first and third dredge-up converts part of their C into N and thus decreasing the $[C/N]$ ratio (see e.g., Masseron & Gilmore 2015). The dependency of the $[C/N]$ ratio at the solar vicinity has been shown to indicate a correlation with stellar ages coming from APOKASC (Martig et al. 2016a) for stars in the $7 < R \text{ (kpc)} < 9$ Galactocentric range. Its usage has been extrapolated to larger disk regions by Ness et al. (2016) and more recently by Hasselquist et al. (2019, 2020), although the dependencies of the $[C/N]$ ratio on metallicity in giants (both through Hot Bottom Burning and stellar yields of C and N), and therefore with the chemical evolution of the Galaxy, makes these extrapolations very uncertain (see Lagarde et al. 2019, for a discussion). Despite these caveats, the $[C/N]$ map in Figure 12 shows an encouraging agreement with previous maps based on the alpha elements, in the sense that larger $[C/N]$ ratios correspond to high $[\alpha/Fe]$ ratios, as expected.

The $[Mn/O]$ ratio also is a very promising population tracer (see Barbuy et al. 2018 for a discussion). This ratio should be low at earlier stages of chemical enrichment, when only core-collapse supernovae had time to pollute the ISM, increasing at later times due to the pollution by SNIa. However, its more complex nucleosynthesis (Chiappini et al. 2003; Barbuy et al. 2013) makes this elemental ratio behave differently from other iron-peak ones (especially, and most importantly, at low metallicities), a fact that enhances differences between separate popula-

tions. An example is illustrated in Figure 12, where a nice correspondence between a low $[Mn/O]$ ratio with the high $[C/N]$ can again be observed. Although, our $[Mn/Fe]$ distribution is biased against very cool stars, since the ASPCAP pipeline cannot measure properly Mn lines for stars with effective temperature below 4000 K. This phenomenon is worse in the case of the RPM sample. Errors due to the assumption of LTE significantly affect data for Mn. Battistini & Bensby (2015) have shown that Mn trends can change drastically if NLTE corrections are taken into account (see also Schultheis et al. 2017).

The $[Mn/O]$ and $[C/N]$ ratios are projected in 2D diagrams in the panels of Figure 14. These panels still show hints of the bimodality observed in the α -elements, despite their more complex nucleosynthesis, the lower statistical significance of these plots, and the larger uncertainties on the measurements of these abundance ratios from APOGEE spectra.

In summary, in this Section we have confirmed that the chemical bimodality previously observed in the alpha elements, is also present in the C/N and Mn/O ratios.

From the standpoint of bulge formation chemodynamical models, the implications differ if one considers that the bimodality is formed by a continuous or two distinct star formation paths. The results presented here, suggest a bimodality with a well defined depression between the two peaks which is more in agreement with a discontinuous star formation path.

Different approaches, going from pure chemical evolution to chemodynamical models (either isolated or in the cosmological scenario) have been explored to understand the observed chemical bimodality first seen around the solar vicinity, and more re-

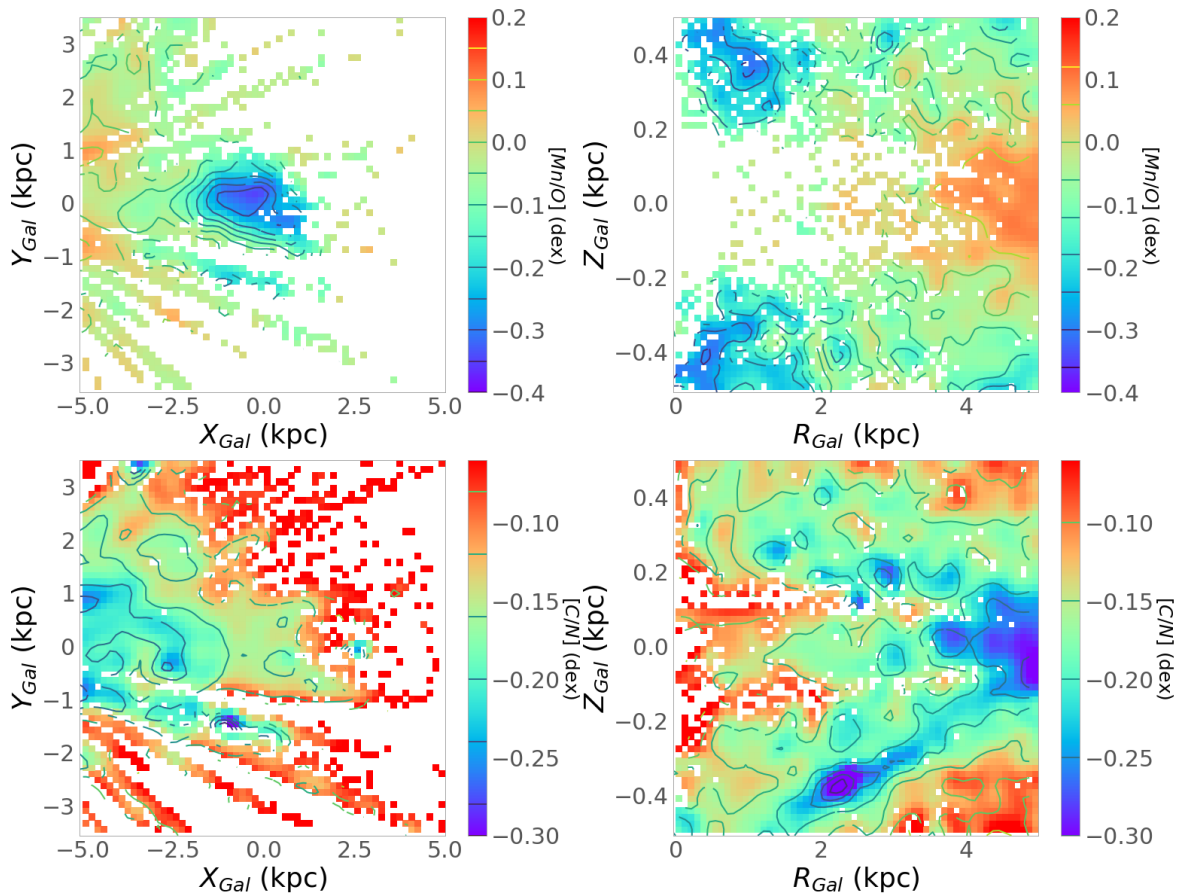


Fig. 12. Same as Figure 7, now colour-coded by [Mn/O] (upper panels) and [C/N] (lower panels).

cently shown to extend towards the whole inner disk (Queiroz et al. 2020) and bulge. These will be discussed in Section 8.

Finally, the chemical maps presented in this section show a consistent picture between the different tracers, and indicate the predominance of a moderately metal-poor, (Barbuy et al. 2018; Savino et al. 2020), population in the innermost Galactocentric regions, which extends to larger Z_{Gal} . This population could be the extension to more intermediate metallicities of the bulge RR Lyrae population discussed in the recent literature (Kunder et al. 2020; Du et al. 2020). We will return to this discussion also in Sec 8. Closer to the Galactic plane, $Z_{Gal} < 300$ pc, the metal-poor population is mixed with a much more metal-rich (and α -poor one) which is very probably related to the rearrangement of disk stars forming a buckling bar. We now proceed to the analysis of the kinematical properties in this region.

6. Kinematics

In Sect. 5 we presented the chemical-abundance distributions of our bulge-bar samples. The clear dichotomy between $[\alpha/Fe]$ -rich/metal-poor and $[\alpha/Fe]$ -poor/metal-rich stars suggests that the Galactic centre region is inhabited by (at least) two very distinct populations. In this section, we analyse the 3D velocity space to establish whether the two distinct chemical populations also present different kinematical properties.

By combining *Gaia* EDR3 and APOGEE data, it has become possible to produce precise three-dimensional kinematic maps that reach even the innermost parts of our Galaxy. Bovy et al. (2019) presented the first Cartesian maps of V_ϕ and V_R using data from APOGEE DR16 coupled with distances obtained using the neural-network algorithm by Leung & Bovy (2019). In

Figure 15 we show X_{Gal} vs Y_{Gal} maps colour-coded by the three velocity components in the Galactocentric cylindrical frame. The maps in Figure 15 cover the bulge-bar sample with a cut in $Z_{Gal} < 0.5$ kpc (lower panels) and an extended region surrounding the Galactic disk (upper panels).

The signature of bar rotation are noticeable in Figure 15. The first panel shows the Cartesian $X - Y$ map colour-coded by V_R . A barred structure is expected to be characterized by a distribution of V_R that extends both inward and outward along the bar. This is seen in simulations of barred galaxies, as discussed in Bovy et al. (2019) and Fragkoudi et al. (2020). This effect is recognized in Figure 15 (first column, lower panel), where the resulting butterfly pattern of the V_R field is clearly observed. A second and more extended quadrupole is seen in the upper panel of Figure 15, indicating the presence of the spiral arms. By comparing the recent maps with simulations, it is possible to characterize the extent of the bar along both the major and minor axis, as well as its angle with the Galactic plane (e.g., Bovy et al. 2019; Hilmi et al. 2020). To guide the eye, in the figures we draw an ellipse with an inclination of 20 degrees in relation to the Sun-GC line, 4 kpc semi-major axis length and 1 kpc semi-minor axis length. A quantitative comparison with models is necessary to fully characterize the Galactic bar.

The second panel of Figure 15 is colour-coded by V_ϕ . It shows a more subtle elliptical shape extending in the X_{Gal} axis by ~ 2 kpc and in the Y_{Gal} axis by ~ 1 kpc, with the V_ϕ growing linearly from 0 to 150 km/s, which is a signature of the rigid body rotation of a barred structure. The elliptical structure in V_ϕ is not as extended and it also is more spherical compared to Bovy et al. (2019).

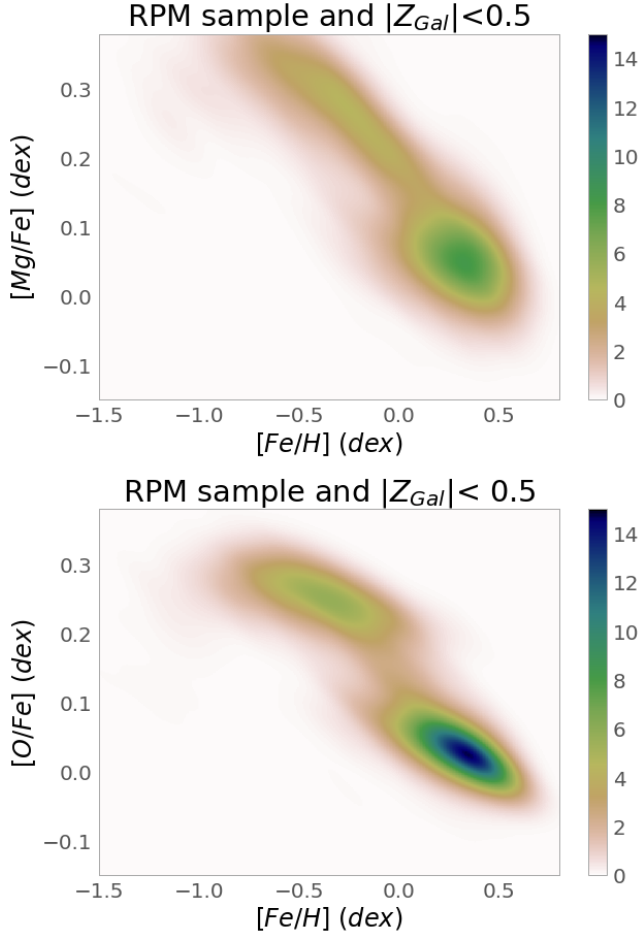


Fig. 13. $[O/Fe]$ vs. $[Fe/H]$ and $[Mg/Fe]$ vs. $[Fe/H]$ for the RPM sample with an extra cut in $|Z_{Gal}| < 0.5$ kpc, respectively. Here too, the figures are colour-coded by the probability density function.

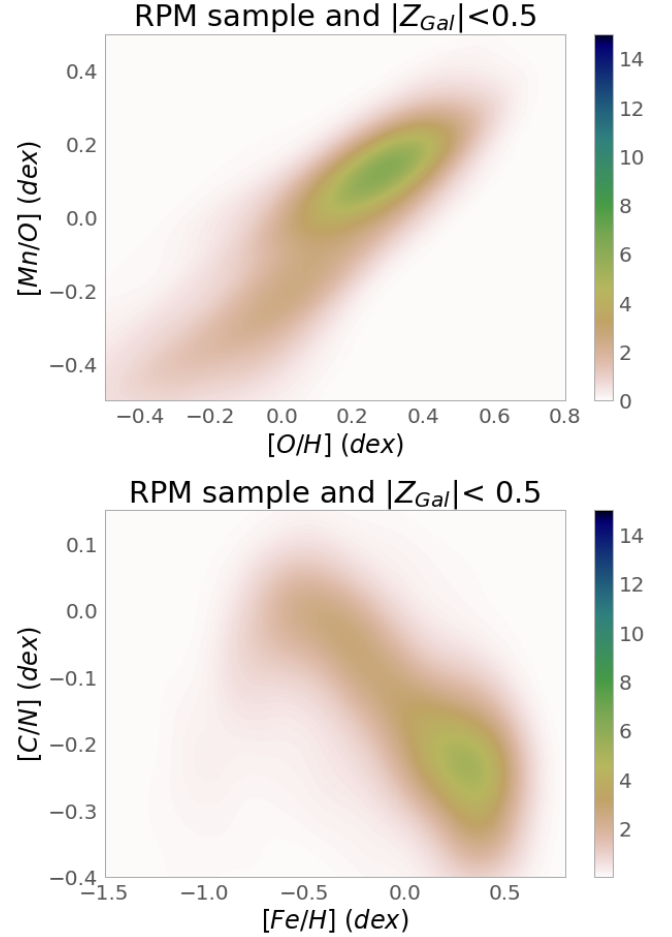


Fig. 14. Two other chemical clocks projected into 2-D diagrams for the RPM sample at $Z_{Gal} > 0.5$ kpc. Upper panel: $[Mn/O]$ vs. $[O/H]$. Lower panel: $[C/N]$ vs. $[Fe/H]$. Here too, the figures are colour-coded by the probability density function.

Finally, in the third panel of Figure 15, we show V_Z . High positive V_Z characterize the region situated on the right side of the ellipse. In contrast, an area with negative V_Z is found at one of the bar ends. In the extended velocity map (third column upper panel) of Fig. 15 it is noticeable positive V_Z in the outer disk, $\sim 10 - 12$ kpc, which was also reported by Carrillo et al. (2019) using *Gaia* DR2 and StarHorse data. The maps shown here show the wave structure in the disk much more clearly, extending the Carrillo et al. (2019) maps to a larger galactocentric range.

In Figure 16 we plot the V_ϕ against the Galactocentric radius, for the bulge-bar sample, and for the RPM selection with an extra cut in the Galactic height ($|Z_{Gal}| < 0.5$ kpc). These diagrams show the clear signature of the distinct stellar populations of a pressure-supported spheroid, a bar, and the Galactic disks. The first panel of Figure 16 shows a population that has a high dispersion in V_ϕ within $R_{Gal} < 1$ kpc and then a structure in which V_ϕ increases linearly with radius, and a third structure with V_ϕ of the order of thin disk population, i.e. ~ 200 km/s. When we apply the RPM cut (second panel of Figure 16), stars with similar Galactic disk V_ϕ decreases significantly, indicating that our selection is indeed culling a more pure bulge-bar sample. Biases must always be considered when analysing kinematics with a previous selection in kinematics, but we would like to remind the reader that the cut in proper motions is subtle, and the velocity distribution of both samples do not change drastically, besides the clear decrease of stars at 200 km/s in $< V_\phi >$. The linear growth of $< V_\phi >$ with R_{Gal} extends up to ~ 4 kpc where there

is a conglomeration of stars that can belong either to the thick disk or to the thin disk.

In order to understand if the kinematical structures seen in Figure 16 do belong to different chemical populations we reproduce in Figure 17 the same plot colour-coded by $[Fe/H]$ and $[\alpha/Fe]$. High metallicity and low- α stars are mostly concentrated around $V_\phi \sim 200$ km/s, again very consistent with what is expected for thin disk stars. Metal-poor and $[\alpha/Fe]$ -rich stars seem to be present in larger fractions inside $R_{Gal} < 1$ kpc and to have a high V_ϕ dispersion, consistent with the expectation for a pressure supported spheroid. One may wonder from the figure, what are the two main concentrations of metal-poor stars, one at negative V_ϕ and one around $V_\phi \sim 100$ km/s. This metal-poor V_ϕ bimodality in Figure 17 is mainly caused by the large contribution of stars at $V_\phi \sim 0$, (see Figure 16). At V_ϕ , $R_{Gal} \sim 0$, a more metal-rich and higher density component dominates, causing the bimodal metal-poor distribution. A bar population signature, where the V_ϕ grows linearly with radius, seems to be complex and characterized by a mixture of both metal-rich and metal-poor populations, it has though a more considerable contribution from metal-rich stars, in agreement with the findings of Wegg et al. (2019), but in contrast to those by Bovy et al. (2019) (see further discussion in Section 7.2). A lump (blob) of high metallicity stars is observed in the right panels of Figure 17, between $10 < V_\phi < 200$ km/s and $R_{Gal} \sim 3.5$ kpc, which possibly represents the contribution of thin and thick disk stars in

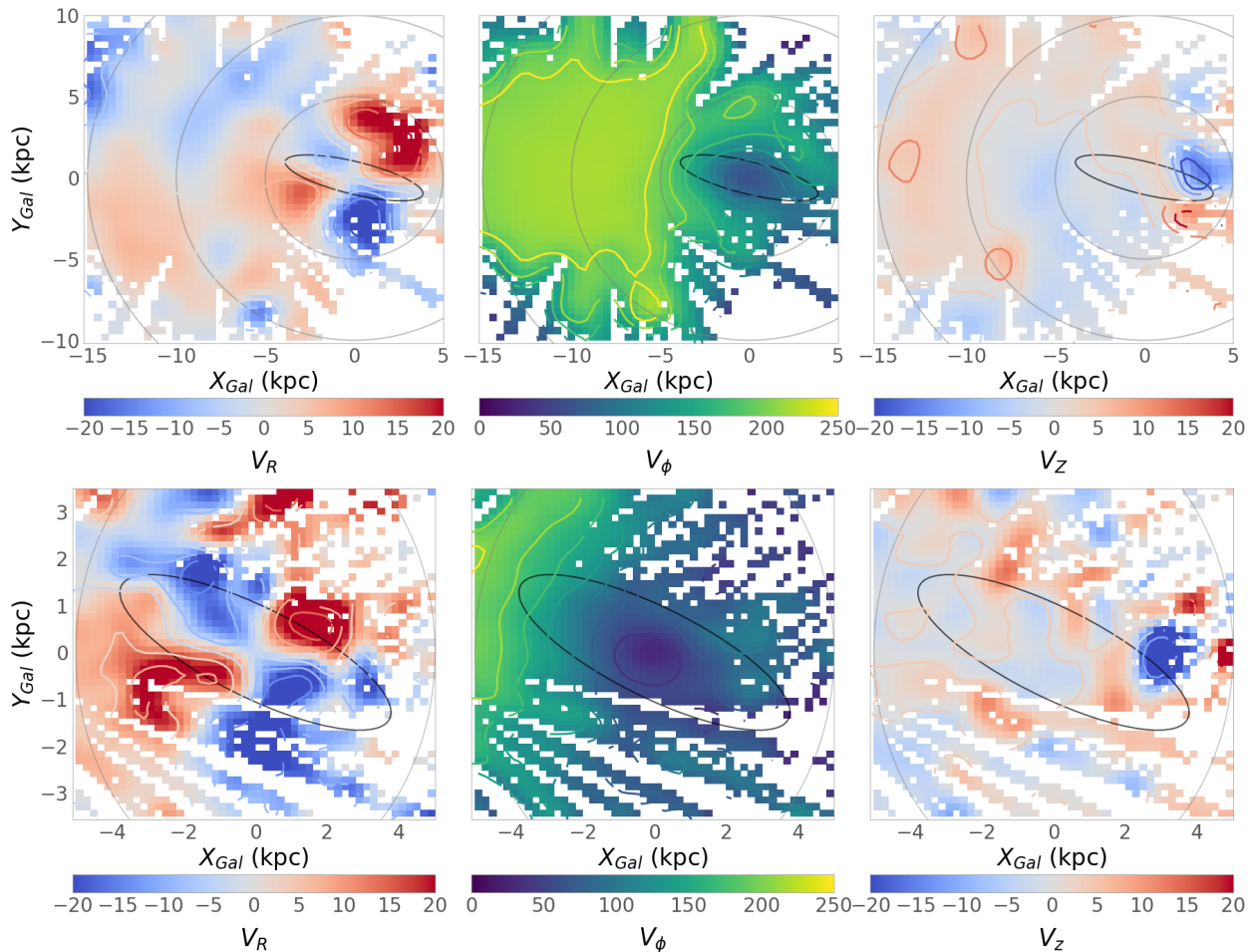


Fig. 15. Cartesian projection of the Galactic disc using StarHorse distances. From left to right the maps are color coded by V_R (first panel), V_ϕ (second panel) and V_Z (last panel). Upper panels show the same region studied in Bovy et al. (2019), while the lower panels zoom-in the innermost 5 kpc of the Galaxy (the grey circles illustrate the galactocentric distances of 5, 10 and 15 kpc).

this region. The maps in this section show the present position of the stars, which means that stars in halo or disk orbits can well be passing close to the Galactic center and be confused with the inner stellar populations in the analysis. With this in mind we proceed to the orbital analysis of its properties as well as its relations to the chemical composition.

7. Dissecting the mixed bulge populations in chemo-orbital parameters

To further disentangle the mixed bulge populations that became evident both during the chemical (see Section 5) and kinematic analysis (see Section 6), we turn to an analysis of the 6D phase space distribution (for a description of the orbital parameters see Section 3) and its relation to stellar chemistry.

7.1. Counter-rotating stars

In Figure 17, we notice a non-negligible contribution of stars with negative V_ϕ , and that is mostly metal-poor. We selected stars with $V_\phi < -50$, from the RPM sample, ~ 600 stars. In the appendix A we show, using Monte Carlo realizations, that simple errors could not reproduce this tail of counter-rotating stars. In Figure 18, we analyse the properties of these stars.

Figure 18 shows the distribution of parameters for stars in our RPM sample with $V_\phi < -50$ km/s in comparison with the

full RPM and bulge-bar samples (limited always to $Z < 0.5$ kpc). The main properties of this retrograde population are:

- Stars with $V_\phi < -50$ km/s are predominantly metal-poor, but show a broad metallicity distribution. The distribution has its highest peak at around $[\text{Fe}/\text{H}] \sim -0.7$, compatible with the metal-poor peak we saw before in the Figure 10 at the inner Galactic centre.
- The mean orbital radius distribution of the $V_\phi < -50$ km/s sample is confined to the innermost 1 kpc Galactocentric range, and the distribution does have large eccentricities.
- Consistent with the fact that it is predominantly metal-poor, the retrograde population is $[\alpha/\text{Fe}]$ -rich and $[\text{C}/\text{O}]$ -poor (i.e., typical of gas mostly polluted by core-collapse supernovae).
- The retrograde stars show larger $[\text{C}/\text{N}]$ ratios, indicative of an older population (made of low mass stars in which hot bottom burning does not take place, and therefore where C did not turn into N in these giants).
- Finally, we show $[\text{Al}/\text{Fe}]$ vs. $[\text{Mg}/\text{Mn}]$ diagram in Figure 19. Our RPM sample automatically excludes most of the more obviously accreted population (in contrast to the sample selection of Horta et al. 2021). According to this criterion the accreted stars are 500 out of 26 500 stars in the Bulge-bar sample, and only 80 out of 8 000 stars in the RPM sample). The blue dots in the right panel of Figure 19 show the locus in the $([\text{Mg}/\text{Mn}], [\alpha/\text{Fe}])$ plane of the counter-rotating stars. These blue dots are dispersed around the whole diagram and are not confined to the accreted location suggested

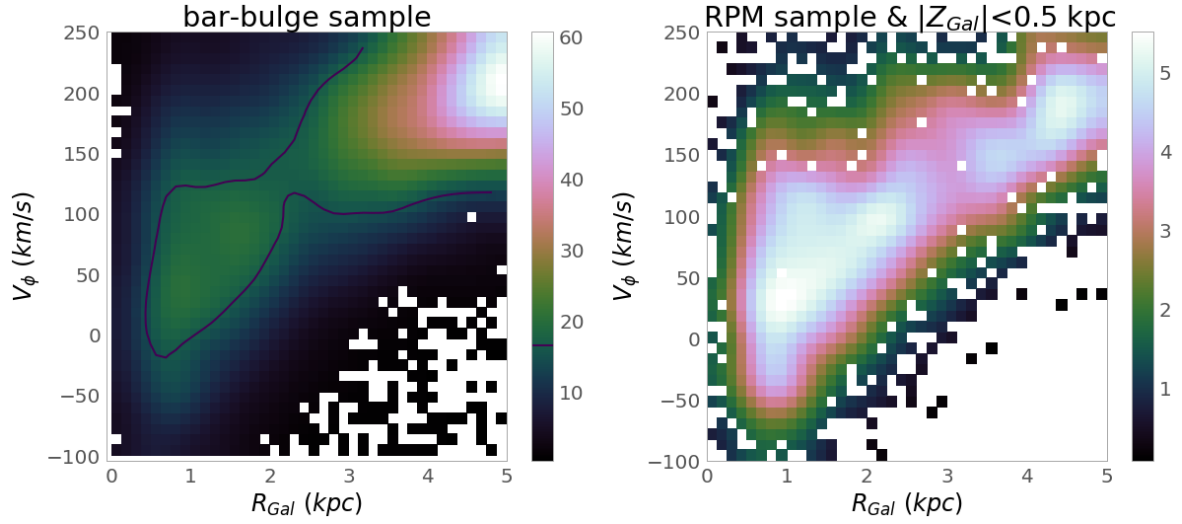


Fig. 16. V_ϕ against Galactocentric radius for the inner Galaxy, the entire bulge-bar sample (left panel) and the RPM with an additional cut in Galactocentric height (right panel). The left panel shows contours of density indicated by the colour bar, highlighting the kinematical populations present in the sample.

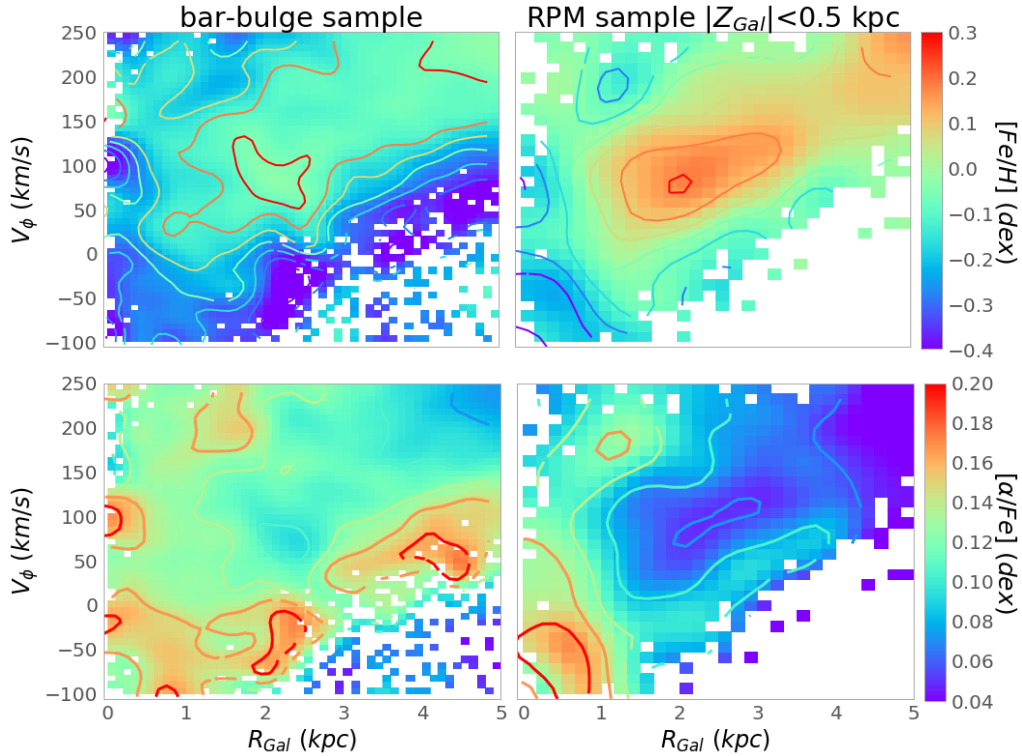


Fig. 17. Same as Figure 16, but now with the panels colour-coded by iron content (upper panels) and α -elements (lower panels).

by Hawkins et al. (2015). As one can notice from the figure, we have checked that the distribution of $[\text{Mg}/\text{Mn}]$ of the retrograde component is shifted to larger values (~ 0.4), whereas a broad range in the values of $[\text{Al}/\text{Fe}]$ is observed than the ones for the accreted location defined by Hawkins et al. (2015).

What could be the origin of this highly eccentric and counter-rotating population confined to the innermost kpc of the Galaxy? One possibility is that this is an accreted metal-poor population, originated during a gas-rich accretion phase in the early formation of the bulge. The metallicity distribution of the retrograde stars includes a metal-rich hump, but this fact could be explained

by some contamination by metal-rich stars. Another interesting possibility is that we are seeing the inner galaxy counterpart of the Splash population identified in the solar vicinity by Belokurov et al. (2020). Splash stars have little to no angular momentum and many are on retrograde orbits and are slightly metal-poor, but can have a broad metallicity range. As explained by the authors there are different theories for the origin of these stars, although the name Splash comes mainly from the idea that these are old stars that belonged to proto-Galactic disk that were dispersed during the accretion event that created the Gaia Sausage. Alternative explanations, however, are also possible. Among them are two very interesting notions that are more directly associated with bulge: a) these stars were formed within

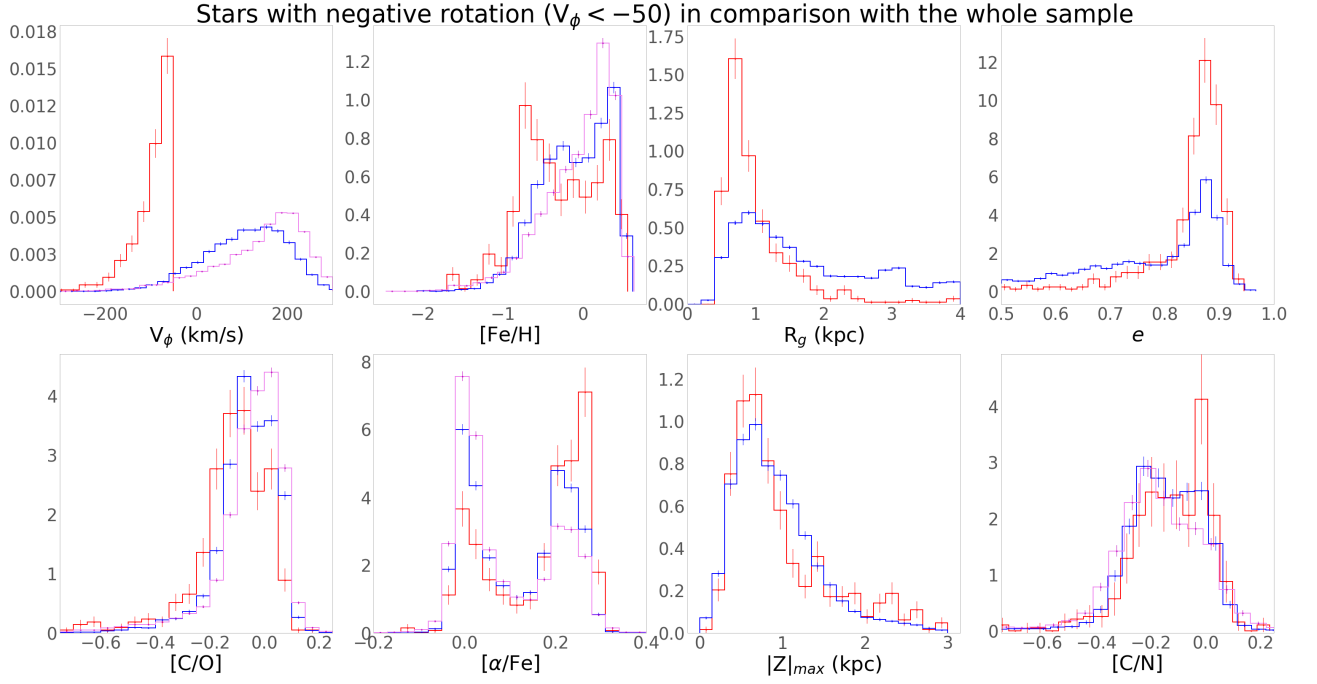


Fig. 18. The distribution of all stars with $V_\phi < -50$ km/s in the RPM sample, shown in red, as a function of many parameters, and compared to the same for all stars in the RPM sample, shown in dark blue, and all stars in the bulge-bar sample, indicated by the violet lines.

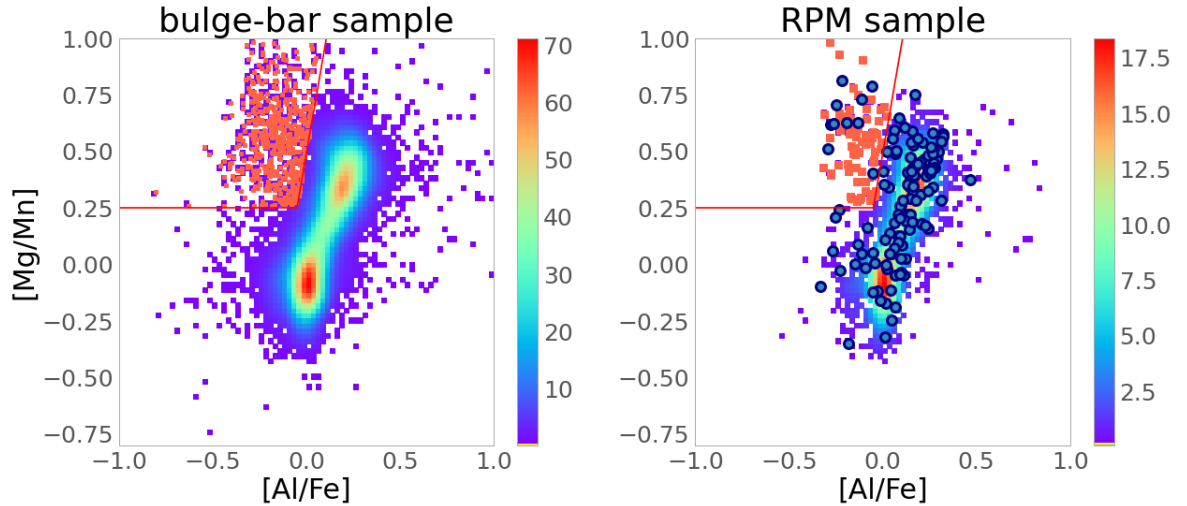


Fig. 19. $[\text{Mg}/\text{Mn}]$ vs. $[\text{Al}/\text{Fe}]$ diagram for bulge-bar sample and RPM samples. The red line indicates the locus of the accreted stars as defined by Hawkins et al. (2015) (see also Das et al. 2020), and the stars that fall in this locus are indicated by the red squares. The blue dots represent the selection of counter-rotating stars, $V_\phi < -50$.

gaseous outflows resulting by a burst in the star-formation or AGN activity (Maiolino et al. 2017; Gallagher et al. 2019), and b) that such retrograde stars in the bulge could be the result of clumps of star formation that took place at early times in the early disk (high redshift) and migrated into the bulge as well as some stars that are driven to retrograde orbits by the bar (Amarante et al. 2020; Fiteni et al. 2021). In both cases, it is expected that a broad velocity dispersion is created, with some stars being on counter-rotating orbits. A recent study analysing the kinematics of metal-poor stars in the inner Galaxy has also find an extended tail of counter-rotating stars which does not match their simulations (Lucey et al. 2021).

Figures 16-19 illustrate the complexity of the Galactic bulge region. On the top of this counter-rotating and/or tail of a hot component we also see the contributions of other populations, with properties suggestive of a bar, an inner-thin disk, a thick

disk and what seems to be a pressure supported component that cannot be attributed to the halo nor to the thick disk. As all these components overlap in the same region and parameter space, neither pure chemical nor kinematical criteria can be used to isolate these different populations. Therefore we turn to a more detailed orbital-chemical analysis. Without pre-selections based on the classical definition of the local Galactic components, we can investigate the dominance of the different components around different parameter ranges.

7.2. The $|Z|_{\text{max}}$ -eccentricity plane

We now turn to the analyses of our RPM sample in the $|Z|_{\text{max}}$ -eccentricity plane, similarly to what has been done in Boeche et al. (2013) and Steinmetz et al. (2020). These papers have

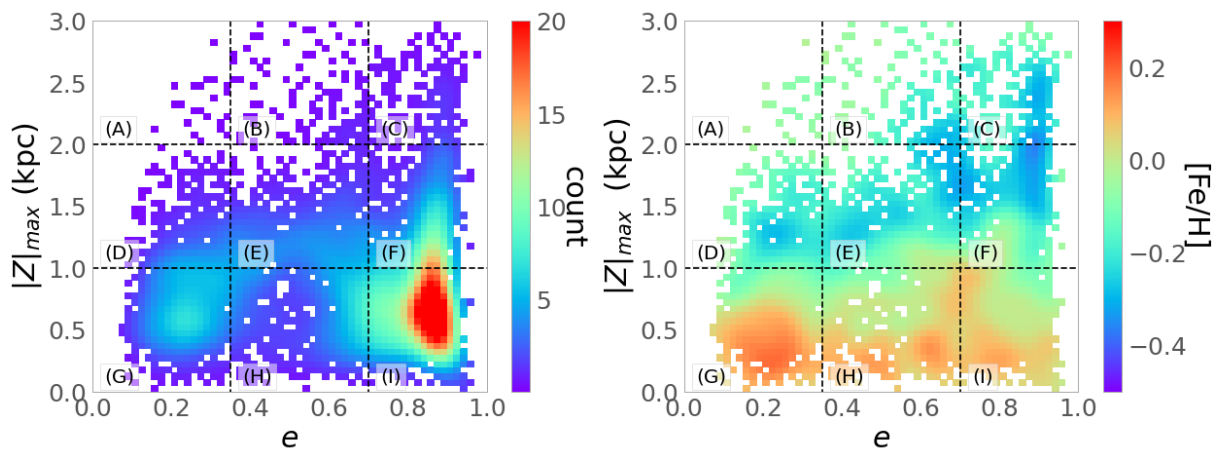


Fig. 20. $|Z|_{\max}$ vs. eccentricity (e) diagram for the RPM sample. In the left panel the colour shows the count of stars per bin and in the right panel the colour shows the mean $[\text{Fe}/\text{H}]$ content per bin. We define nine windows in this diagram indicated by the letters (A) to (I).

shown that this parameter space offers a powerful way to disentangle the coexisting populations in the region (therefore avoiding the use of pre-define Galactic populations based on properties of the more local samples).

Figure 20 shows the distribution of stars in this plane colour-coded by number density (left panel), and by metallicity (right panel). We divide the $|Z|_{\max}$ -eccentricity plane into nine cells (referenced by the alphabetic labels in the figure). From these diagrams we notice that most stars from our RPM sample have high eccentricity and low $|Z|_{\max}$. A second prominent population is concentrated at very low eccentricities and low $|Z|_{\max}$, being mostly composed by high metallicity stars, which is consistent with classical disk populations. The right panel of Figure 20 is dominated by a metallicity gradient away from the mid-plane. On top of this there is a population of less metal-rich stars on highly eccentric orbits that reaches to ~ 1 kpc in $|Z|_{\max}$. Is also noticeable a deficit of stars at intermediate eccentricities ~ 0.48 . Next, we analyse the composition distribution and orbital parameters for each cell.

Figure 21 shows $[\alpha/\text{Fe}]$ vs. $[\text{Fe}/\text{H}]$ for each cell defined in Fig. 20. Note that this is different than the usual diagram seen in bins of R , Z (e.g. Hayden et al. 2015; Queiroz et al. 2020). Here instead we are focusing on a very inner sample, and mapping the chemistry of stars sampling different orbital parameter space in that inner region. It shows that low- $[\alpha/\text{Fe}]$ stars are on low-inclination orbits, while high- α stars are on orbits of all types. Both populations are spread over orbits of every eccentricity.

Cell (I) shows a hot population (eccentricities > 0.7) with thin-disk-like low- $[\alpha/\text{Fe}]$ on the top of a more metal-poor, high- α population. As we will see next, the stars in this cell are mostly stars on bar-shape orbits. As we go to higher $|Z|_{\max}$ we lose most of the low- $[\alpha/\text{Fe}]$ stars, which results in the metallicity gradient seen in the right panels of Figure 20. The separation between high- $[\alpha/\text{Fe}]$ and low- $[\alpha/\text{Fe}]$ is also clear in cell (I), whereas the bimodality becomes less clear for smaller eccentricities and higher $|Z|_{\max}$.

The high- $[\alpha/\text{Fe}]$ population shows a broad range of metallicities for the cells at high eccentricity (especially at low $|Z|_{\max}$), and gradually becomes narrower towards low eccentricities. The cells (G) and (D) are consistent with predominantly thin and chemical-thick disk populations, respectively, with their distributions of $[\alpha/\text{Fe}]$ vs. $[\text{Fe}/\text{H}]$ appearing to be similar to those in Nidever et al. (2014); Hayden et al. (2015); Queiroz et al. (2020) for intermediate Galactocentric radii $4 < R_{\text{gal}} < 10$ kpc.

However, for stars on more eccentric orbits (cells C, F and I), the high- $[\alpha/\text{Fe}]$ populations become more extended in metallicity. One way of interpreting this is that the so-called knee moves to larger values for these stars. This is, for instance, the behavior predicted for a spheroidal bulge (e.g., Matteucci et al. 2020, Cescutti et al. in prep). Moreover, these cells show slightly larger $[\alpha/\text{Fe}]$ than the ones more chemical-thick disk-like dominated. Notice that this is not in contradiction with earlier APOGEE results showing that the high- $[\alpha/\text{Fe}]$ chemical-thick-disk component has the same shape in different $R_{\text{gal}}-Z_{\text{gal}}$ bins. It is just that now we are able to see a spheroidal population confined to the smallest R_{mean} , which stands out among the more eccentric stars. This suggests that the chemical-thick disk and spheroidal bulge have slightly different $[\alpha/\text{Fe}]$ -enhancements (see Barbuy et al. 2018, for a discussion). We also should keep in mind that cells (G), (H), (I) may be incomplete, because of the selection outside the heavily reddened regions as seen in Sec. 2.

To understand where bar-like orbits would fall in these diagrams we made Figure 22 which shows the $[\alpha/\text{Fe}]$ vs. $[\text{Fe}/\text{H}]$ similarly to Figure 21, but now colour-coded by the probability of the star to be in a bar-shape orbit. To estimate this probability, we used the Monte Carlo sample of each star (50 orbits, see Sec. 3) and calculated the fraction of orbits classified as a bar-shape orbit. To classify each orbit, we follow the definition from Portail et al. (2015) which uses frequency analysis. We compute the main frequencies of each orbit in the Cartesian coordinate x and the cylindrical radius R in the bar frame. The orbits for which the frequency ratio $fR/fx = 2 + / - 0.1$ are in a bar-shape orbit. The orbits that are not in a bar-shape orbit have a frequency ratio $fR/fx \neq 2 + / - 0.1$.

Figure 22 shows that the stars most likely to be on bar-shaped orbits are in the cell (I), with important contribution also in the cell (H). As expected, the stars on the bar show eccentric and low $|Z|_{\max}$ orbits. One very important result is that the stars following the bar orbits in cells (I) and (H) are found both on the low- and high- α populations. This fact suggests stellar trapping to have been an efficient mechanism along the bar lifetime, bringing to the bar stars that had previously belonged to Galactic components formed even before the bar was formed. There is a clear dearth of stars on bar orbits at high $|Z|_{\max}$ and low eccentricity.

Figures 23 and 24 show the distributions of metallicity and R_{mean} , for each $|Z|_{\max}$ -eccentricity cell. These figures show very interesting features that are related to what we see in Figure 21 of the $[\alpha/\text{Fe}]$ vs. $[\text{Fe}/\text{H}]$ discussed above, namely:

- In Fig. 23 we see two populations, one with a narrow $[\text{Fe}/\text{H}]$ centred on ≈ 0.2 and the other a broader distribution centred on ≈ -0.7 . Comparison of Figures 21 & 23 tells us that the former is the low-alpha population and the latter the high-alpha population.
- The high $[\alpha/\text{Fe}]$ cells (I), (F) and (C) span the widest range of metallicities, but a narrower range in R_{mean} , with most stars with $R_{\text{mean}} < 3$ kpc. The sampled R_{mean} go from $R_{\text{mean}} < 2$ kpc (I) to $1 < R_{\text{mean}} < 3$ kpc, as we go up in $|Z|_{\text{max}}$. That is of course expected, but what is interesting is that this is accompanied by a low metallicity component that starts to become more prominent (going from cells I to C). As will be shown, these high-eccentricity stars are composed of a mix of the bar and spheroid populations, giving the impression of a metallicity gradient with $|Z|_{\text{max}}$. The peak in the metallicity of cell (C) is consistent with the metal-poor one seen in Figure 10.
- The metallicity distribution clearly becomes narrower toward lower eccentricities, while the distribution in R_{mean} is now broader, and with fewer stars coming from the innermost kiloparsecs.
- In the bottom row ($|Z|_{\text{max}} < 1$), the prominent high metallicity peak goes from $[\text{Fe}/\text{H}] \sim 0.25$ in cell (I), to 0.2 in cells (G) and (H). Progressively, going from (I) to (G) one also sees that the metal-poor population around -0.7 dex gets weaker (with fewer and fewer stars from the pressure supported component which is composed mostly by stars with $R_{\text{mean}} < 3$ kpc). This is the population that is very dominant in cells (I), (F) and (C) as discussed before. Still in the bottom row, going from (I) to (G), a peak at $[\text{Fe}/\text{H}] \sim -0.3$ gets more prominent. This peak will increase for intermediate eccentricities as one goes up in $|Z|_{\text{max}} < 1$. One can see that this corresponds mostly to stars with $2 \text{ kpc} < R_{\text{mean}} < 3 \text{ kpc}$.
- For low eccentricity stars (left columns in Figures 23 and 24), the mean orbital radius distributions get broader, with $R_{\text{mean}} > 2$ kpc. This suggests the inner disk stars were not born in the innermost 2 kpc of the Galaxy, a result reminiscent of that by Matsunaga et al. (2016) based on classical Cepheids (see discussion in Section 7). The metallicity distribution is now dominated by stars in the $3 \text{ kpc} < R_{\text{mean}} < 4 \text{ kpc}$ mean orbital radius range, and a peak around -0.27 dex starts to appear. In cell (G), the contribution of three peaks is visible at $[\text{Fe}/\text{H}] \sim 0.2, -0.27$ and -0.33 dex. Toward larger $|Z|_{\text{max}}$ values, the metal-rich peak disappears, and the other two start dominating, consistent with a transition from a thin-disk like population to a chemical-thick disk population.

By analysing Figures 23 and 24, now together with the V_ϕ distributions (Figure 25), we can more quantitatively relate the populations discussed previously.

- It is possible to see the contributions from the chemically defined inner thin and thick disks in Figures 24 and 25, in cells (G),(D),(A) (left column of the $|Z|_{\text{max}}$ -eccentricity diagram). The first column of the diagram is mostly dominated by inner thin disk stars (stars with a V_ϕ peak at around 200 km/s and the low V_ϕ dispersion).
- The second column of the $|Z|_{\text{max}}$ -eccentricity diagram (intermediate eccentricities) contains mostly chemical-thick disk-like stars, which become more dominant towards larger $|Z|_{\text{max}}$ values (also confirmed by the metallicity distribution in Figure 23).
- The last column of the $|Z|_{\text{max}}$ -eccentricity diagram (highly eccentric orbits) selects a pressure supported component, with lower rotation and larger V_ϕ dispersion (with small angular momentum and therefore small R_g range), which we saw in Fig. 21 to be a metal-poor, high- $[\alpha/\text{Fe}]$ population.

- At low $|Z|_{\text{max}}$ and high eccentricity (cell I), the bar population starts dominating over the spheroid (pressure-supported population described in the previous bullet), increasing the metallicity (as we also saw from the bar probability figure.)
- The last column also reveals, superposed with the spheroid and bar populations (both having large eccentricities) the counter-rotating, metal-poor population discussed in Section 7.1. Here, it is more prominent at the highest $|Z|_{\text{max}}$ cell, probably because at lower $|Z|_{\text{max}}$ it gets buried in the much more dominant metal rich population of the bar. The counter-rotating population could also just be an extended tail of the spheroid. In the Appendix A we show that the errors are not likely to form an asymmetric structure in V_ϕ , significantly that would extend to high negative rates such as -50 km/s.
- We also notice positive tails in the centre 3 panels of Figure 25. The canonical V_ϕ distribution of an exponential disc has a sharp cutoff at high V_ϕ , suggesting a slow outward decline in σ_R .

In summary, the analysis performed in this Section shows, for the first time, a detailed dissection of the innermost parts of the Milky Way. We show the several peaks in the metallicity distribution to actually correspond to populations of different eccentricities and $|Z|_{\text{max}}$ distributions. The metal-rich population (with a peak at 0.2 dex) is made of inner thin disk stars, mostly formed outside the innermost 1-2 kpc. Part of the metal-rich stars are from the bar, which is populated by stars with R_{mean} within the 0-3 kpc range. These populations sit on top of a broader metallicity component extending from around -0.8 to over-solar, which resembles a classical bulge (Cescutti et al. 2018; Matteucci et al. 2019) made of mostly high- $[\alpha/\text{Fe}]$ stars (most probably old - see Miglio et al. 2021). Meanwhile, with increasing $|Z|_{\text{max}}$ one starts to probe even more of the inner chemical-thick disk, and the metallicity distribution gets more and more dominated by stars with metallicities around -0.5 dex, which is similar to the peak of the local thick disk metallicity distribution (emerging in cell (B)).

8. Summary and Implications

In this paper we have analysed the inner regions of our Galaxy using APOGEE post-DR16 internal release data combined with *Gaia* EDR3 and with the StarHorse distances and extinctions. This latter addition provides us with an unprecedented catalogue of the Galactic innermost regions, with thousands of stars having distance uncertainties smaller than 1 kpc.

We analyse two distinct samples: a) one sample of more than 26 500 stars spatially selected in Cartesian coordinates X and Y , and b) a sample of around 8 000 stars, more confined to the inner Galaxy and cleaned from foreground stars by using the RPM method, which becomes possible thanks to *Gaia* EDR3 very precise proper motions. Most of this sample is outside the locus for accreted stars defined by Hawkins et al. (2015); Das et al. (2020) on the $[\text{Mg}/\text{Mn}]-[\text{Al}/\text{Fe}]$ plane (but see discussion in Horta et al. 2021). Despite this we see a counter-rotating population the origin of which has to be further investigated (see discussion in Section 7.1).

With our larger sample we were able to build exquisite chemical and kinematical maps of the innermost regions of the Galaxy. The chemical data show that:

- A clear chemical bimodality is present in the $[\alpha/\text{Fe}]$ vs. $[\text{Fe}/\text{H}]$ diagram for the full 26 500 stars sample. The separation becomes more evident when we apply a proper motion cut to clean the sample for foreground disk stars. Although the bimodality has also been detected in previous

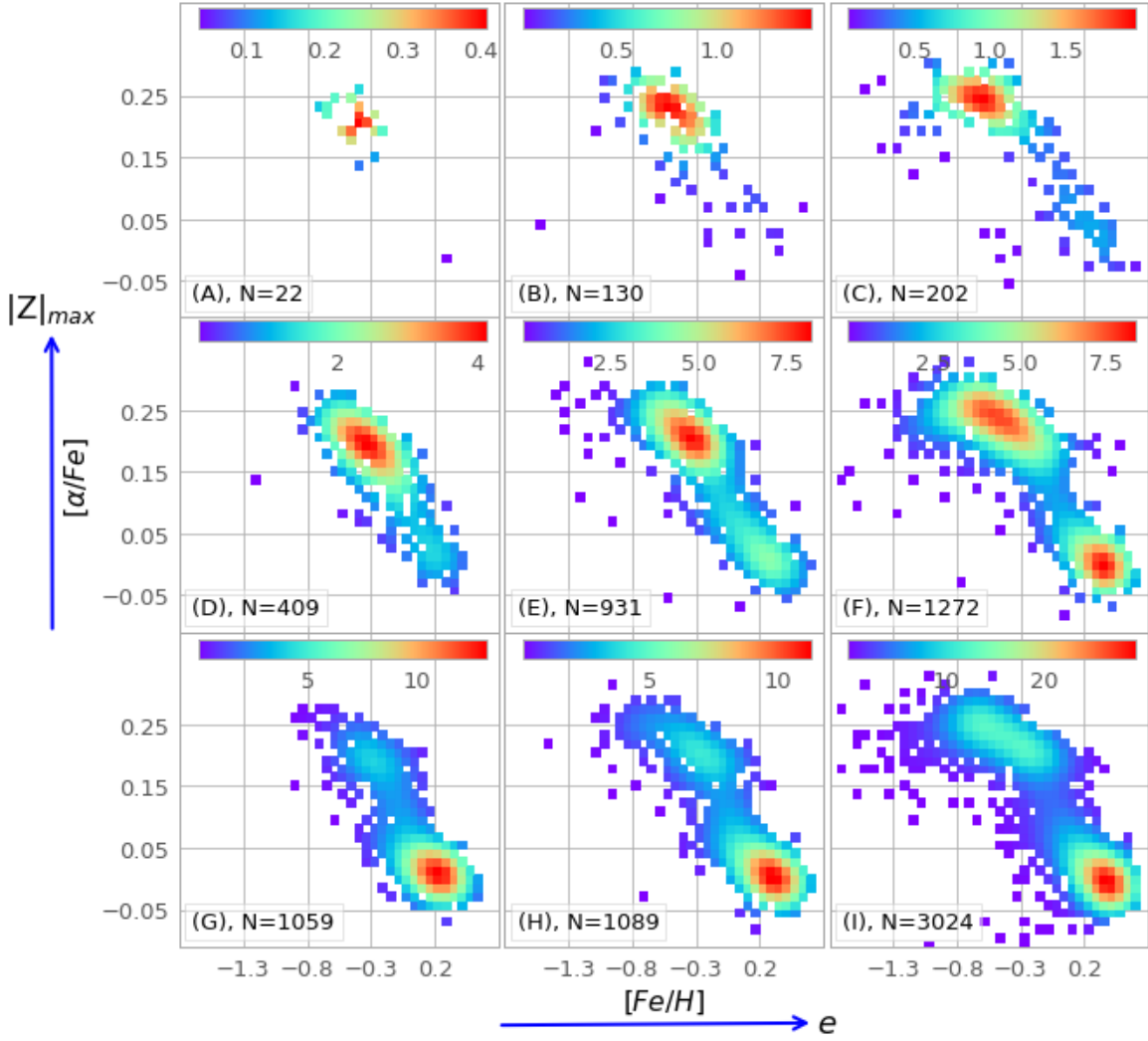


Fig. 21. $[\alpha/\text{Fe}]$ vs. $[\text{Fe}/\text{H}]$ for each cell defined in Fig. 20. The number of stars for each cell is indicated next to the panel labels. The rightmost columns, dominated by large eccentricity stars (pressure-supported component), show larger alpha-enhancement ($[\alpha/\text{Fe}] \sim 0.25$), than what is seen among the low-eccentricity stars. The (inner) thin disk contribution is seen mostly in the lower row, with a low, near-solar $[\alpha/\text{Fe}]$ ratio, which peaks at $[\text{Fe}/\text{H}] = 0.2$ in cells (G) and (H), and at 0.25 in cell (I).

works (Rojas-Arriagada et al. 2019; Queiroz et al. 2020) it is much more clearly seen here. We also confirm that similar results are obtained when we adopt $[\text{Mg}/\text{Fe}]$ or $[\text{O}/\text{Fe}]$. This shows the level of precision and consistency obtained by the APOGEE ASPCAP pipeline (García Pérez et al. 2016; Jönsson et al. 2020).

- In chemical evolution it is expected that a bimodality seen in $[\alpha/\text{Fe}]$ vs. $[\text{Fe}/\text{H}]$, is also seen in other chemical abundance ratios that trace similar enrichment timescales. Here we illustrate this by using the $[\text{C}/\text{N}]$ and $[\text{Mn}/\text{O}]$ ratios. Indeed, double densities are also seen when they are plotted as a function of metallicity. For the C/N ratio the interpretation is complex as both elements can be modified during the evolution of the star on the giant branch. For $[\text{Mn}/\text{O}]$ difficulties arise in the abundance measures because the pipeline processing does not estimate Mn for stars cooler than 4000 K. But broadly the results are consistent with the bimodality seen in alpha-elements.
- The chemical maps show a spatial dependency on the metallicity, with the predominance of a metal-poor (α -rich) component that is located in the central region. This feature can now be seen in the XY plane. This component is also seen on the $[\text{C}/\text{N}]$ and $[\text{Mn}/\text{O}]$ maps, again in agreement with nu-

cleosynthetic sites of production of these different elements, and their release timescales to the interstellar medium.

- The XY spatial maps of cylindrical velocities exhibit an elliptical but almost circular form in V_ϕ and a butterfly pattern in V_R , indicating the rotation of a barred structure, i.e. the kinematical signature of a bar. This is similar to what has been seen by Bovy et al. (2019), also using DR16 data but with fewer stars and a completely different way of estimating distances. The velocity maps are in agreement with the expectation from simulations of barred galaxies e.g., as discussed by several authors (Debattista et al. 2017; Bovy et al. 2019; Carrillo et al. 2019; Fragkoudi et al. 2020), where the butterfly pattern of the V_R field is one example of the expected features. These maps suggest an inclination of the bar with the Galactic plane of 20 degrees, spatial extent of around 4 kpc in the semi-major axis and 1 kpc in the semi-minor axis. A more detailed comparison with models is required to provide a more quantitative characterization of the properties of the Milky Way bar.
- The V_ϕ against Galactocentric radius (mapped both in $[\alpha/\text{Fe}]$ and $[\text{Fe}/\text{H}]$) for the two samples studied here, show the signature of the distinct stellar populations coexisting in these samples, suggesting the presence of a pressure-supported

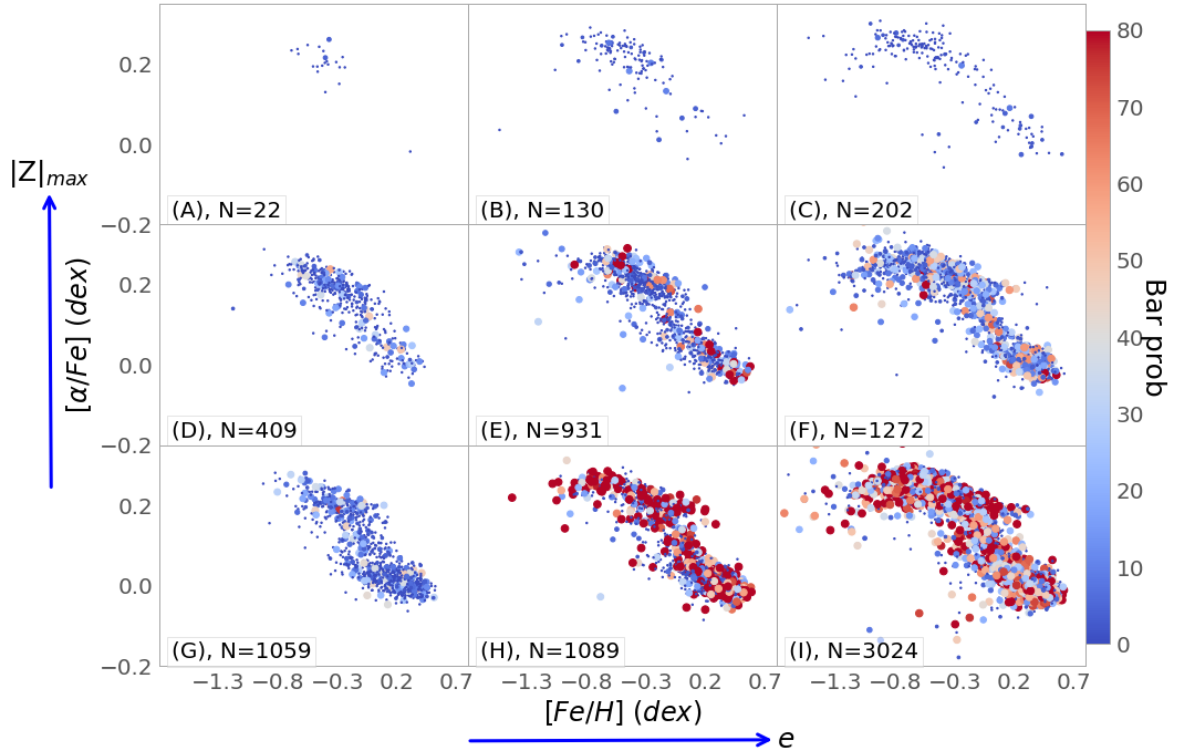


Fig. 22. $[\alpha/\text{Fe}]$ vs. $[\text{Fe}/\text{H}]$ for each cell defined in Figure 20 now colour-coded by the star's probability to follow a bar orbit (see text). Stars with the largest bar-shape orbit probabilities populate cells (H) and (I), and are found both among high- and low- $[\alpha/\text{Fe}]$ populations.

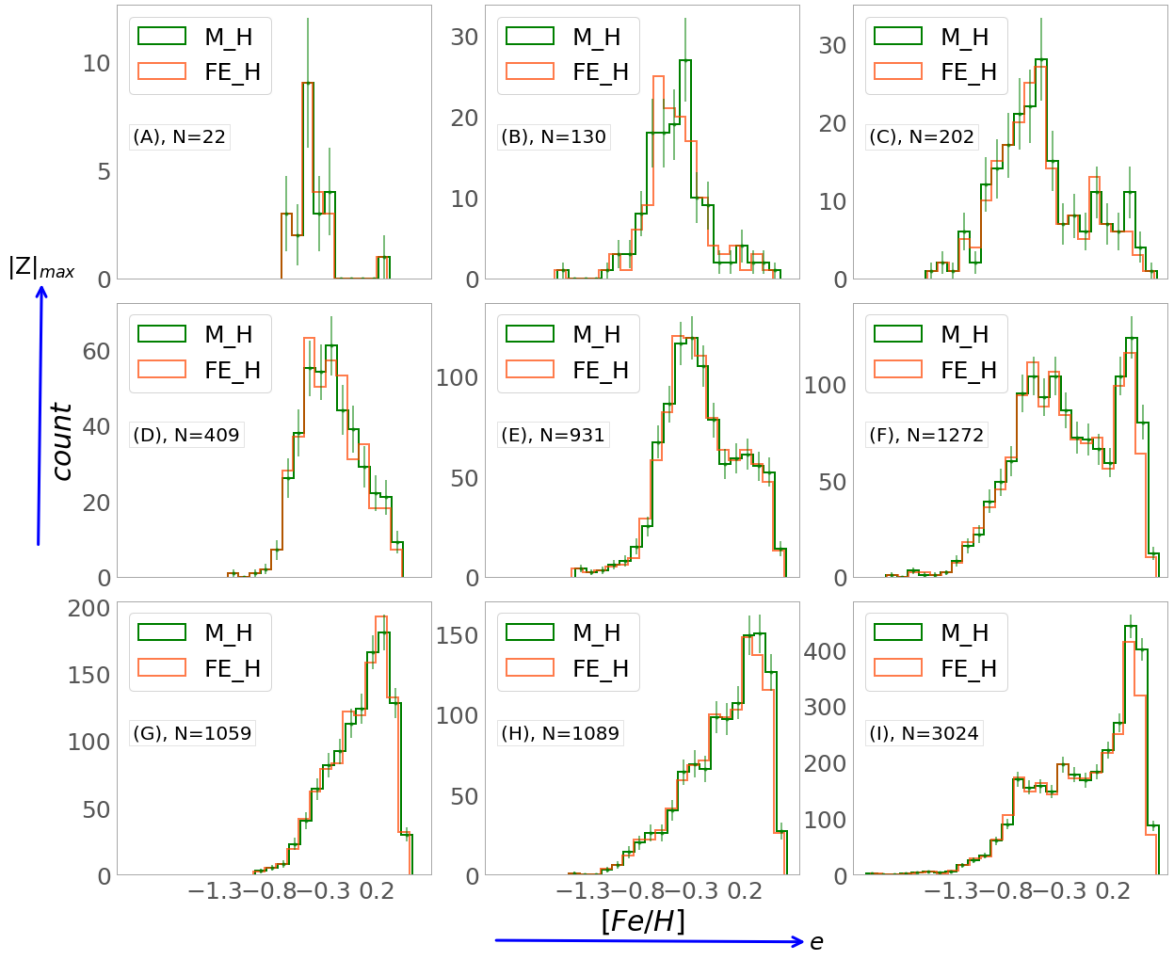


Fig. 23. Metallicity distribution function for each cell defined in Fig. 20. We show the distributions of $[\text{Fe}/\text{H}]$ (orange line) and $[\text{M}/\text{H}]$ (green line) coming from ASPCAP.

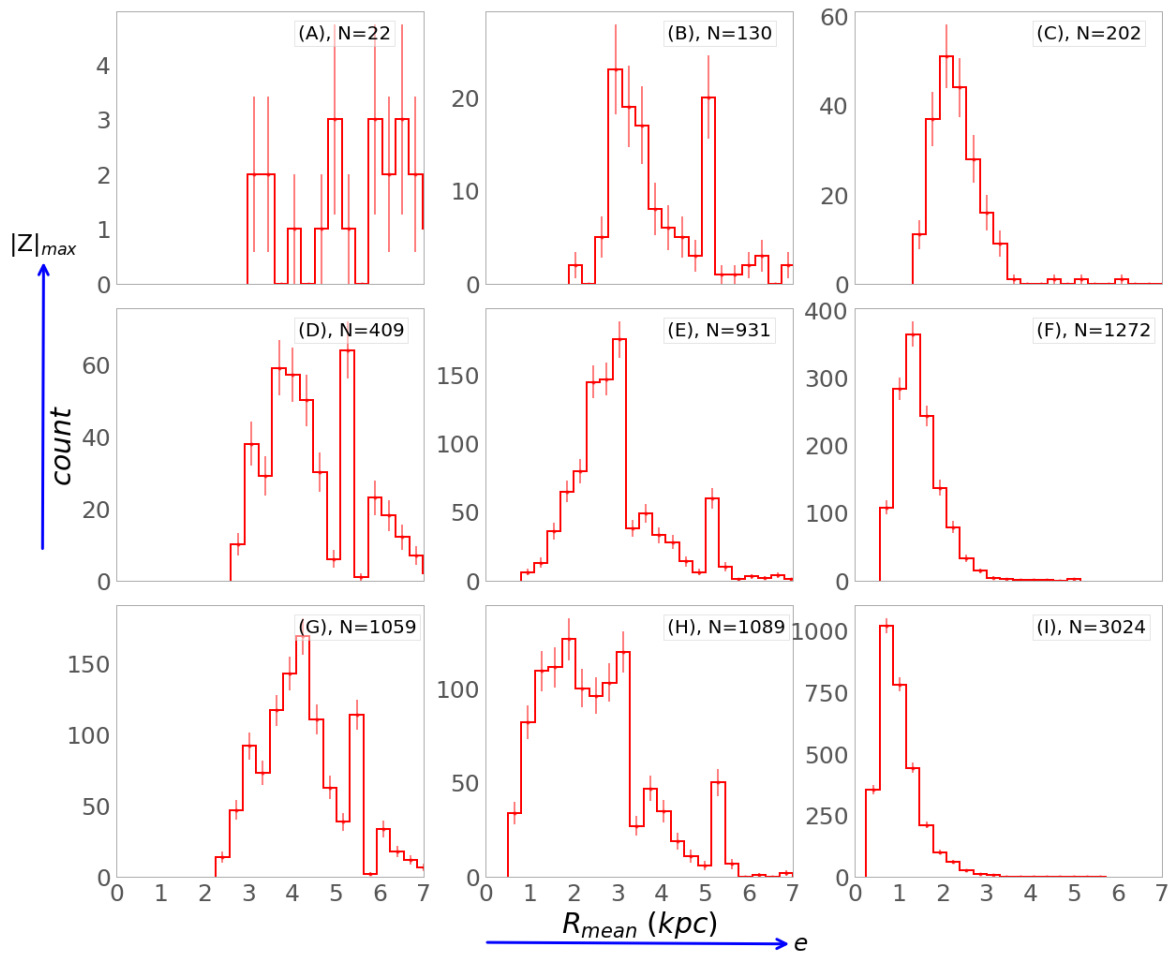


Fig. 24. Mean orbital radii distribution for each cell defined in Figure 20. The more eccentric population has R_{mean} confined to the innermost (1-3 kpc) regions of the Galaxy, whereas the thin disk stars have R_{mean} larger than 2-2.5 kpc.

spheroid, a bar, and the Galactic disks. These diagrams also show a counter-rotating population of metal-poor stars or an extended tail of negative V_ϕ , which we then characterize in detail. In particular, the dispersion in V_ϕ of the innermost metal-poor component is too large to be attributed to thick disk stars (around 120 km/s), strongly suggesting the presence of an underlying spheroid, as predicted by Minniti (1996).

After the chemical and the velocity analysis we further dissect the innermost regions thanks to a sample of approximately 8 000 stars for which we computed stellar orbits. The populations are then characterized on a $|Z|_{\text{max}}$ -eccentricity plane (and in this way we avoid any pre-selection based on chemistry or kinematics). We pursue a joint analysis of the distributions of metallicity, $[\alpha/\text{Fe}]$ abundance ratios, mean orbital radii (R_{mean})¹, and the V_ϕ and its dispersion. This comprehensive analysis is needed in order to map the parameter space where each of the different populations dominate, thus avoiding the use of artificial sharp boundaries definitions. In this way we identify and better characterize the chemical properties of the following populations inhabiting the innermost parts of the Milky Way close to the Galactic midplane:

¹ R_{mean} represents the mean galactocentric distance a star has in its orbit, i.e., the mean between its apocentric and pericentric distances). This is here taken as being close to the birthplace of the stars, except for effects due to radial migration.

– Inner thin-disk and the bar:

Most of the low eccentricity, high V_ϕ stars show low- $[\alpha/\text{Fe}]$. This inner thin disk population has a metallicity peak at $[\text{Fe}/\text{H}] = +0.2$. This metallicity shifts to larger values for more eccentric stars, still close to the Galactic midplane, reaching a peak of $[\text{Fe}/\text{H}] = +0.25$. These metallicities however are seen only in the (1-2) kpc mean orbital radius range, suggesting that the most metal-rich stars are part of the bar component (in agreement with Wegg et al. (2019)). This suggests the bar to be slightly more enriched than the inner thin disk stars, most probably due to residual star formation in the innermost 2 kpc that form stars that get into bar orbits. Bars at high redshift could induce burst of star formation due to gas trapping and gas funneling, especially toward the center. The inner-thin disk stars in our sample have R_{mean} larger than 3 kpc, consistent with the fact that the thin disk does not extend all the way to the Galactic center (although this conclusion could be affected by the non optimal coverage of the inner most regions). This is in agreement with a similar suggestion made by Matsunaga et al. (2016) who reported that no Cepheid was found in the innermost 2.5 kpc of the Milky Way.

– Pressure supported component and the bar: Underneath the bar population mostly found at large eccentricities and low heights from the plane (confirmed by the large fraction of stars with bar-shape orbits in this part of the parameter space - see Figure 22), there is another component that is much broader in metallicity and that becomes more apparent as

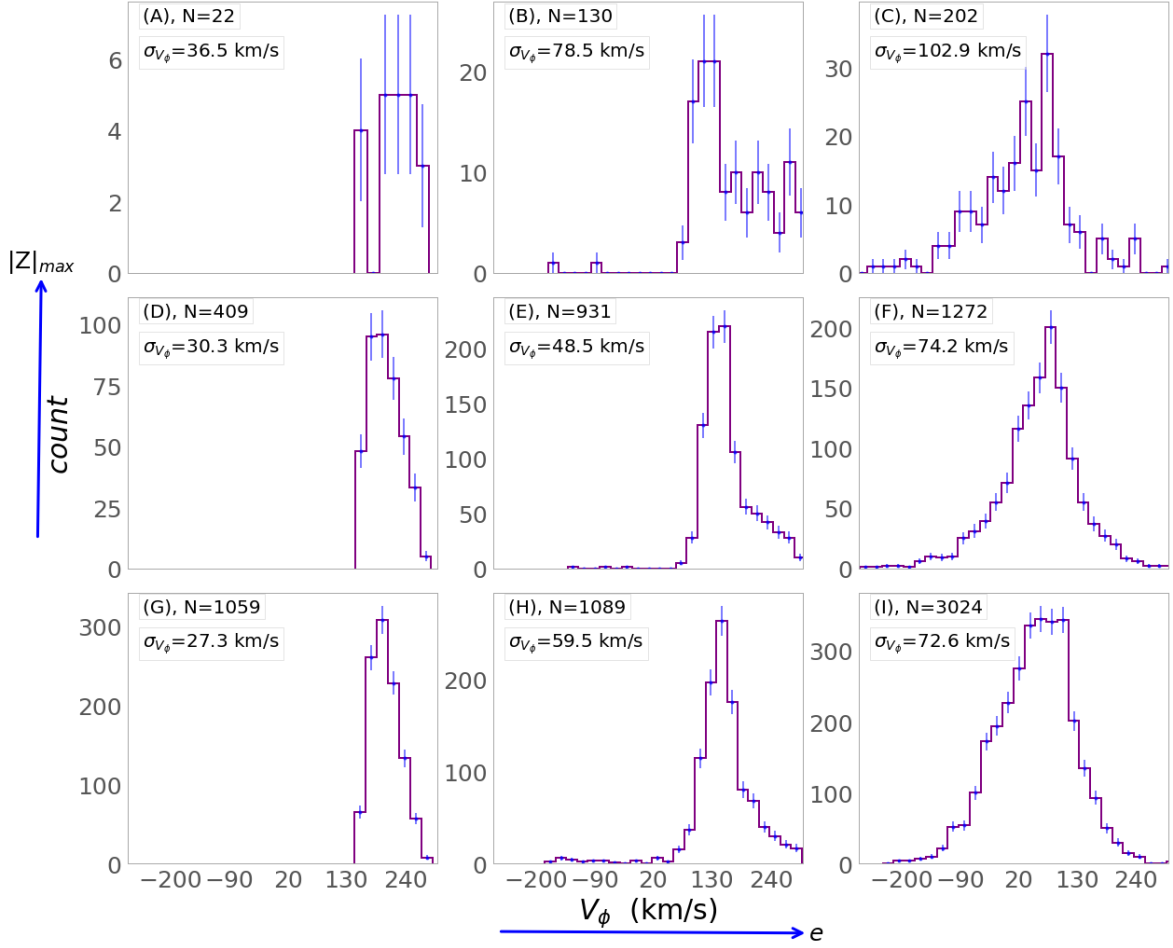


Fig. 25. V_ϕ distribution for each cell defined in Figure 20. The value of the dispersion in V_ϕ is also shown for each cell. Thick disk with $V_\phi \sim 140$ km/s are seen in panels H and E where there is less contamination by thin disk (with V_ϕ around 200 km/s - cells G and D) and the spheroidal component (with V_ϕ around 80 km/s cells I, F and C). A counter-rotating tail is noticeable in cell C.

one goes towards larger distances from the Galactic mid-plane (where the bar component fade in). This large velocity dispersion component has a non-negligible contribution of metal-poor stars, which makes the metallicity distribution broad. This pressure-supported spheroid shows high- $[\alpha/\text{Fe}]$ ratios values. Part of these spheroid stars that have orbits more confined to lower heights from the Galactic midplane also get trapped by the bar. Indeed, as shown in Figure 22) we find stars with a high probability of being in bar-shaped orbits among the high- $[\alpha/\text{Fe}]$ stars. This figure suggests bar stars have eccentricities in the 0.5-0.8 range and metallicities above solar (explaining the shift to larger metallicities in cell (I) of Figure 23). Therefore, we find the bar to be composed mostly by metal-rich stars, with some additional contribution of stars with similar chemical pattern of those in the spheroidal component. The latter were most probably trapped into the bar potential. It seems that the bar traps the more metal-rich component of the spheroid, while the more metal-poor one is able to escape the bar. The mechanisms to explain how this happens need to be investigated by proper dynamical models. This also explains the details of the shape of the $[\alpha/\text{Fe}]$ vs. $[\text{Fe}/\text{H}]$ distribution closer to the Galactic midplane, which becomes more metal rich both in high and low-alpha populations.

- Inner chemical thick disk: Stars of intermediate eccentricities, with V_ϕ compatible with the local chemical-thick disk population, dominate cell (E) (Fig. 23 and Fig. 25). These

stars also show typical local chemical-thick disk metallicity distribution (Fig. 23) and $[\alpha/\text{Fe}]$ enhancement.

The majority of these stars are not on bar-shape orbits. Local chemical-thick disks stars were recently shown to be a very old and coeval population (thanks to the very precise ages from asteroseismology (see Miglio et al. 2021; Montalbán et al. 2021)). Therefore the same is expected to be true for the inner-thick disk population discussed here. If that is the case, it would suggest this component to have formed before the bar.

- Counter-rotating stars or the tail of the pressure supported (spheroid) component: We find, superposed on the two components populating the high eccentricity orbits (the bar and the pressure-supported spheroid), a population with negative V_ϕ , in highly eccentric orbits, confined to the innermost kpc of the Galaxy. This population is seen as a tail in the V_ϕ distribution shown in cell C of Figure 25, and its properties are shown in Figure 18. Given the low statistics of stars in cell C, a more robust characterization of this population is deferred for future work which will be able to use larger samples.
- The spheroid and the thick disk: The conclusion that we have a non-negligible contribution from a spheroid (on the top of the thick disk like component) is strengthened by the shape of the high-alpha populations in Figure 21. One sees that the high- $[\alpha/\text{Fe}]$ population is shifted to slightly larger values of $[\alpha/\text{Fe}]$ in the last column of the figure (spheroid-dominated), compared to the ones on the two other columns (more thick-

disk dominated). Also the extent of the high- α population is different, going to larger metallicities for the spheroidal-dominated population, suggesting larger star formation rate (and efficiency) in the spheroidal bulge than in the thick disk. The caveat here is that this can also be the result of low statistics in the thick-disk dominated cells. A more detailed comparison between these two populations, with more data, will be the topic of a forthcoming paper.

8.1. Potential impact

The existence of an spheroidal bulge, in which star formation has been vigorous would be in agreement with what is expected from chemical evolution models (see a discussion in Section 4 of Barbuy et al. (2018), and Matteucci et al. (2019)). In a scenario of fast enrichment, very old stars can be found already at metallicities $[\text{Fe}/\text{H}] \sim -1$ (see Chiappini et al. (2011); Wise et al. (2012); Cescutti et al. (2018) and Section 3.2.4 of Barbuy et al. (2018) for a discussion). Indeed, some of the oldest objects known in our Galaxy are located in the bulge and, have metallicities around one-tenth of solar. For instance, the Galactic bulge has a system of globular clusters (Minniti 1995) that are now known to be among the oldest in our Galaxy (Barbuy et al. 2009; Chiappini et al. 2011; Barbuy et al. 2014; Kerber et al. 2018, 2019; Ortolani et al. 2019). These can be as old as the RR Lyrae. These stars were born around 400 thousand years after the Big Bang, and are thus relics of the earliest chemical enrichment of the Universe.

The properties of the pressure supported metal-poor, α -enhanced stars we find in the bulge, are consistent with the RR Lyrae stars in the same region. A debate around the origin of the RR Lyrae population in the bulge has been ongoing, and the conclusions are very dependent on the samples analysed and models employed. Some of the suggestions in the literature are that these RR Lyrae could be the extension of the stellar halo in the inner Galaxy (Minniti 1996; Pérez-Villegas et al. 2017a), have a bar distribution (Pietrukowicz et al. 2015), or give evidence of being a more spheroidal, concentrated, pressure-supported structure (Dékány et al. 2013; Kunder et al. 2016; Contreras Ramos et al. 2018). To break this dichotomy, Kunder et al. (2020) recently suggest the existence of two components of RR Lyrae in the inner Galaxy. One RR Lyrae component is spatially and kinematically consistent with the bar, and the second component is more centrally concentrated and does not trace the bar structure. This agrees with the results shown here, where we see that the bar seems to trap mostly thin disk stars, but also the more metal-rich part of the α -enhanced spheroidal component.

The pressure-supported component could be the result of an accreted event, or strong gas flows, at the early stage of the Galaxy's formation, and this is consistent with an age for the RR Lyrae stars in the bulge of 13.41 ± 0.54 Gyr (Savino et al. 2020). Du et al. (2020) use OGLE IV photometry and Gaia DR2 proper motions to analyze metal-poor ($[\text{Fe}/\text{H}] < -1$) and metal-rich ($[\text{Fe}/\text{H}] > -1$) RR Lyrae stars in the bulge. They concluded that the angular velocities and spatial distribution are different between metal-rich and metal-poor RR Lyrae stars. These results are in agreement with Wegg et al. (2019) and Kunder et al. (2020).

The results presented here also offer some insight on the conundrum of the age of the bulge, namely: the old ages from color magnitude diagrams proper motion cleaned towards low extinction bulge windows, versus the non-negligible contribution of stars younger than 5 Gyr suggested by the microlensed dwarfs (Bensby et al. 2017). After the analysis shown here, it is clear

that each of the techniques lead to a different mixture of stars — the Baade's window CMD probing more of the spheroidal component mostly occurring in the inner 2-3 kpc of the Galaxy, whereas in the other case the stars are sampling a mix of spheroidal and inner thin disk stars, as confirmed by their multi-peak metallicity distribution (see also Rojas-Arriagada et al. 2020).

The clear bimodality in the chemical diagrams for stars closer to the Galactic mid-plane, and the existence of a dearth of stars in between the two overdensities (Fig. 13), offer an important new observational constraint to chemo-dynamic models of the Galaxy. There has been considerable debate on the origin of this bimodality based on data more close to the solar vicinity and since the proposition made more than 20 years ago by (Chiappini et al. 1997) that this would reflect two main star formation paths, with a quenching of the star formation in between. More recently, this scenario has been revived both by chemical evolution models and numerical simulations (e.g. Anders et al. 2017, 2018; Weinberg et al. 2019; Spitoni et al. 2021; Grand et al. 2020) as well as by the indication of an age dichotomy between the high- and low- α populations (Miglio et al. 2021; Rendle et al. 2019; Lian et al. 2020; Das et al. 2020). Cosmological simulations are particularly important to identify the reasons for this quenching, which can be manifold as discussed in the literature (e.g., Weinberg et al. 2019; Grand et al. 2020; Agertz et al. 2020; Ciuca & Hernández 2020; Buck 2020; Vincenzo & Kobayashi 2020). Alternative views, explaining the observed dichotomy as being the result of internal processes such as radial migration were also put forward (Schönrich & Binney 2009; Sharma et al. 2020), but difficulties in forming a hot thick disk like component just by radial migration have been pointed out (for a discussion Minchev et al. 2013; Martig et al. 2016b; ?, see) The data presented here for the innermost regions now show the dichotomy to be present also in the innermost regions. The properties of the different populations show the dichotomy to be mainly a result of the mix of different populations. The upper $[\alpha/\text{Fe}]$ -sequence is dominated by an spheroidal, pressure-supported component (the bulge) in the innermost 2-3 kpc, whereas it is dominated by thick disk stars beyond that distance. The lower sequence is formed by the bar in the innermost 2-3 kpc, and then by thin disk stars not in the bar. Further out, the lower α -sequence is then the result of the thin disk mixture caused by radial migration from stars born at different galactocentric distances (Friedli et al. 1994; Minchev et al. 2013, 2014). Stars born at different distances have different chemistry due to the inside out formation of the disk. Note however, that the chemical bimodality is less clear in the high-resolution data towards Baade's window (as can be seen in Barbuy et al. (2018)). However, in a recent study by Thorsbro et al. (2020) a chemical bimodality is also detected. Accurate distances are necessary to put these findings on more solid grounds. One caveat we still have to consider is that even though StarHorse provides a large improvement in distance and extinction estimates, it still does not take into account variations on the extinction law, which are potentially important in the bulge region. Improvements in this direction are also part of our future plans.

Finally, we also see a population of counter-rotating stars, which needs to be further investigated and confirmed. This population could be the remnant of an early accretion event, or the coalescence into the forming bulge of a clump of star formation formed by disk instabilities Elmegreen et al. (2008); Huertas-Company et al. (2020) like those commonly observed in the disks of star-forming galaxies at redshift $z \sim 2-3$. Otherwise it could just be the tail of the large dispersion spheroid.

APOGEE plus Gaia have been transformative in our understanding of the innermost parts of the Milky Way. The picture

emerging from our results is in much better agreement with high-redshift observations, which show early spheroids being formed due to massive amounts of highly dissipative gas accretion and mergers as suggested by simulations (e.g. Tacchella et al. 2015; Bournaud 2016; Renzini et al. 2018).

Acknowledgements

The authors thank the referee, Prof. James Binney, for all the valuable suggestions. The authors thank R. Schiavon for helpful discussions. CC acknowledges support from DFG Grant CH1188/2-1 and from the ChETEC COST Action (CA16117), supported by COST (European Cooperation in Science and Technology). FA is grateful for funding from the European Union's Horizon 2020 research and innovation programme under the Marie Skłodowska-Curie grant agreement No. 800502 H2020-MSCA-IF-EF-2017. BB acknowledges partial financial support from FAPESP, CNPq, and CAPES - Finance Code 001. APV acknowledges the FAPESP postdoctoral fellowship no. 2017/15893-1 and the DGAPA-PAPIIT grant IG100319. DAGH acknowledges support from the State Research Agency (AEI) of the Spanish Ministry of Science, Innovation and Universities (MCIU) and the European Regional Development Fund (FEDER) under grant AYA2017-88254-P. ARA acknowledges partial support from FONDECYT through grant 3180203. J.G.F-T is supported by FONDECYT No. 3180210 and Becas Iberoamérica Investigador 2019, Banco Santander Chile. S.H. is supported by an NSF Astronomy and Astrophysics Postdoctoral Fellowship under award AST-1801940. SH is supported by an NSF Astronomy and Astrophysics Postdoctoral Fellowship under award AST-1801940. ABAQ, CC, FA, BX, BB acknowledges support from Laboratório Interinstitucional de e-Astronomia (LIneA).

This work has made use of data from the European Space Agency (ESA) mission *Gaia* (<http://www.cosmos.esa.int/gaia>), processed by the *Gaia* Data Processing and Analysis Consortium (DPAC, <http://www.cosmos.esa.int/web/gaia/dpac/consortium>). Funding for the DPAC has been provided by national institutions, in particular the institutions participating in the *Gaia* Multilateral Agreement.

The *StarHorse* code is written in python 3.6 and makes use of several community-developed python packages, among them *astropy* (Astropy Collaboration et al. 2013), *ezpadova*, *numpy* and *scipy* (Virtanen et al. 2019), and *matplotlib* (Hunter 2007). The code also makes use of the photometric filter database of VOSA (Bayo et al. 2008), developed under the Spanish Virtual Observatory project supported from the Spanish MICINN through grant AyA2011-24052.

Funding for the SDSS Brazilian Participation Group has been provided by the Ministério de Ciência e Tecnologia (MCT), Fundação Carlos Chagas Filho de Amparo à Pesquisa do Estado do Rio de Janeiro (FAPERJ), Conselho Nacional de Desenvolvimento Científico e Tecnológico (CNPq), and Financiadora de Estudos e Projetos (FINEP).

Funding for the Sloan Digital Sky Survey IV has been provided by the Alfred P. Sloan Foundation, the U.S. Department of Energy Office of Science, and the Participating Institutions. SDSS-IV acknowledges support and resources from the Center for High-Performance Computing at the University of Utah. The SDSS web site is www.sdss.org.

SDSS-IV is managed by the Astrophysical Research Consortium for the Participating Institutions of the SDSS Collaboration including the Brazilian Participation Group, the Carnegie Institution for Science, Carnegie Mellon University, the Chilean Participation Group, the French Participation Group, Harvard-Smithsonian Center for Astrophysics, Instituto de Astrofísica de Canarias, The Johns Hopkins University, Kavli Institute for the Physics and Mathematics of the Universe (IPMU) / University of Tokyo, Lawrence Berkeley National Laboratory, Leibniz-Institut für Astrophysik Potsdam (AIP), Max-Planck-Institut für Astronomie (MPIA Heidelberg), Max-Planck-Institut für Astrophysik (MPA Garching), Max-Planck-Institut für Extraterrestrische Physik (MPE), National Astronomical Observatory of China, New Mexico State University, New York University, University of Notre Dame, Observatório Nacional / MCTI, The Ohio State University, Pennsylvania State University, Shanghai Astronomical Observatory, United Kingdom Participation Group, Universidad Nacional Autónoma de México, University of Arizona, University of Colorado Boulder, University of Oxford, University of Portsmouth, University of Utah, University of Virginia, University of Washington, University of Wisconsin, Vanderbilt University, and Yale University.

References

- Abolfathi, B., Aguado, D. S., Aguilar, G., et al. 2018, *ApJS*, 235, 42
- Agertz, O., Pontzen, A., Read, J. I., et al. 2020, *MNRAS*, 491, 1656
- Ahumada, R., Allende Prieto, C., Almeida, A., et al. 2020, *ApJS*, 249, 3
- Amarante, J. A. S., Beraldo e Silva, L., Debattista, V. P., & Smith, M. C. 2020, *ApJ*, 891, L30
- Anders, F., Chiappini, C., Minchev, I., et al. 2017, *A&A*, 600, A70
- Anders, F., Chiappini, C., Santiago, B. X., et al. 2014, *A&A*, 564, A115
- Anders, F., Khalatyan, A., Chiappini, C., et al. 2019, *A&A*, 628, A94
- Anders, F., Queiroz, A. B., Chiappini, C., et al. 2018, in *IAU Symposium*, Vol. 334, *Rediscovering Our Galaxy*, ed. C. Chiappini, I. Minchev, E. Starkenburg, & M. Valentini, 153–157
- Arenou, F., Luri, X., Babusiaux, C., et al. 2018, *A&A*, 616, A17
- Arentsen, A., Starkenburg, E., Martin, N. F., et al. 2020, *MNRAS*, 491, L11
- Astropy Collaboration, Robitaille, T. P., Tollerud, E. J., et al. 2013, *A&A*, 558, A33
- Baade, W. 1946, *PASP*, 58, 249
- Babusiaux, C. 2016, *PASA*, 33, e026
- Babusiaux, C., Gómez, A., Hill, V., et al. 2010, *A&A*, 519, A77
- Babusiaux, C., Katz, D., Hill, V., et al. 2014, *A&A*, 563, A15
- Barbuy, B., Chiappini, C., Cantelli, E., et al. 2014, *A&A*, 570, A76
- Barbuy, B., Chiappini, C., & Gerhard, O. 2018, *ARA&A*, 56, 223
- Barbuy, B., Hill, V., Zoccali, M., et al. 2013, *A&A*, 559, A5
- Barbuy, B., Zoccali, M., Ortolani, S., et al. 2009, *A&A*, 507, 405
- Battistini, C. & Bensby, T. 2015, *A&A*, 577, A9
- Bayo, A., Rodrigo, C., Barrado Y Navascués, D., et al. 2008, *A&A*, 492, 277
- Belokurov, V., Sanders, J. L., Fattahi, A., et al. 2020, *MNRAS*, 494, 3880
- Bennett, M. & Bovy, J. 2019, *MNRAS*, 482, 1417
- Bensby, T., Feltz, S., Gould, A., et al. 2017, *A&A*, 605, A89
- Bernard, E. J., Schultheis, M., Di Matteo, P., et al. 2018, *MNRAS*, 477, 3507
- Bland-Hawthorn, J. & Gerhard, O. 2016, *ARA&A*, 54, 529
- Blanton, M. R., Bershad, M. A., Abolfathi, B., et al. 2017, *AJ*, 154, 28
- Boeche, C., Chiappini, C., Minchev, I., et al. 2013, *A&A*, 553, A19
- Bournaud, F. 2016, *Astrophysics and Space Science Library*, Vol. 418, *Bulge Growth Through Disc Instabilities in High-Redshift Galaxies*, ed. E. Laurikainen, R. Peletier, & D. Gadotti, 355
- Bovy, J., Leung, H. W., Hunt, J. A. S., et al. 2019, *MNRAS*, 490, 4740
- Buck, T. 2020, *MNRAS*, 491, 5435
- Buck, T., Ness, M., Obreja, A., Macciò, A. V., & Dutton, A. A. 2019, *ApJ*, 874, 67
- Cao, L., Mao, S., Nataf, D., Rattenbury, N. J., & Gould, A. 2013, *MNRAS*, 434, 595
- Carrillo, I., Minchev, I., Steinmetz, M., et al. 2019, *MNRAS*, 490, 797
- Cescutti, G., Chiappini, C., & Hirschi, R. 2018, in *IAU Symposium*, Vol. 334, *Rediscovering Our Galaxy*, ed. C. Chiappini, I. Minchev, E. Starkenburg, & M. Valentini, 94–97
- Chambers, K. C., Magnier, E. A., Metcalfe, N., et al. 2016, *arXiv e-prints*, arXiv:1612.05560
- Cheng, X. in prep., *Exploring the Galactic Warp Through Asymmetries in the Kinematics of the Galactic Disk*
- Chiappini, C., Frischknecht, U., Meynet, G., et al. 2011, *Nature*, 472, 454

- Chiappini, C., Matteucci, F., & Gratton, R. 1997, *ApJ*, 477, 765
- Chiappini, C., Romano, D., & Matteucci, F. 2003, *MNRAS*, 339, 63
- Ciuca, R. & Hernández, O. F. 2020, *MNRAS*, 492, 1329
- Contreras Ramos, R., Minniti, D., Gran, F., et al. 2018, *ApJ*, 863, 79
- Cunha, K. & Smith, V. V. 2006, *ApJ*, 651, 491
- Cutri, R. M., Skrutskie, M. F., van Dyk, S., et al. 2003, 2MASS All Sky Catalog of point sources.
- Cutri, R. M., Wright, E. L., Conrow, T., et al. 2013, Explanatory Supplement to the AllWISE Data Release Products, Tech. rep.
- Das, P., Hawkins, K., & Jofré, P. 2020, *MNRAS*, 493, 5195
- Debattista, V. P., Ness, M., Gonzalez, O. A., et al. 2017, *MNRAS*, 469, 1587
- Dehnen, W. 2000, *AJ*, 119, 800
- Dékány, I., Minniti, D., Catelan, M., et al. 2013, *ApJ*, 776, L19
- Du, H., Mao, S., Athanassoula, E., Shen, J., & Pietrukowicz, P. 2020, arXiv e-prints, arXiv:2007.01102
- Eisenstein, D. J., Weinberg, D. H., Agol, E., et al. 2011, *AJ*, 142, 72
- Elmegreen, B. G., Bournaud, F., & Elmegreen, D. M. 2008, *ApJ*, 688, 67
- Faherty, J. K., Burgasser, A. J., Cruz, K. L., et al. 2009, *AJ*, 137, 1
- Fernández-Trincado, J. G., Beers, T. C., Minniti, D., et al. 2021, *A&A*, 647, A64
- Fernández-Trincado, J. G., Beers, T. C., Minniti, D., et al. 2020a, *A&A*, 643, L4
- Fernández-Trincado, J. G., Beers, T. C., Placco, V. M., et al. 2019a, *ApJ*, 886, L8
- Fernández-Trincado, J. G., Chaves-Velasquez, L., Pérez-Villegas, A., et al. 2020b, *MNRAS*, 495, 4113
- Fernández-Trincado, J. G., Zamora, O., Souto, D., et al. 2019b, *A&A*, 627, A178
- Ferrers, N. 1877, the Potentials of Ellipsoids, Ellipsoidal Shells, Elliptic Laminæ, and Elliptic Rings of Variable Densities.
- Fiteni, K., Caruana, J., Amarante, J. A. S., Debattista, V. P., & Beraldo e Silva, L. 2021, *MNRAS*, 503, 1418
- Fragkoudi, F., Grand, R. J. J., Pakmor, R., et al. 2020, *MNRAS*, 494, 5936
- Friça, A. C. S. & Barbuy, B. 2017, *A&A*, 598, A121
- Friedli, D., Benz, W., & Kennicutt, R. 1994, *ApJ*, 430, L105
- Fulbright, J. P., McWilliam, A., & Rich, R. M. 2007, *ApJ*, 661, 1152
- Gaia Collaboration, Brown, A. G. A., Vallenari, A., et al. 2018, *A&A*, 616, A1
- Gaia Collaboration, Brown, A. G. A., Vallenari, A., et al. 2020, arXiv e-prints, arXiv:2012.01533
- Gallagher, R., Maiolino, R., Belfiore, F., et al. 2019, *MNRAS*, 485, 3409
- García Pérez, A. E., Allende Prieto, C., Holtzman, J. A., et al. 2016, *AJ*, 151, 144
- García Pérez, A. E., Ness, M., Robin, A. C., et al. 2018, *ApJ*, 852, 91
- Gontcharov, G. A. 2009, *Astronomy Letters*, 35, 638
- Gonzalez, O. A., Rejkuba, M., Zoccali, M., et al. 2013, *A&A*, 552, A110
- Gonzalez, O. A., Rejkuba, M., Zoccali, M., et al. 2012, *A&A*, 543, A13
- Gonzalez, O. A., Zoccali, M., Vazquez, S., et al. 2015, *A&A*, 584, A46
- Gran, F., Minniti, D., Saito, R. K., et al. 2015, *A&A*, 575, A114
- Grand, R. J. J., Kawata, D., Belokurov, V., et al. 2020, *MNRAS*, 497, 1603
- Gunn, J. E., Siegmund, W. A., Mannery, E. J., et al. 2006, *AJ*, 131, 2332
- Hasselquist, S., Holtzman, J. A., Shetrone, M., et al. 2019, *ApJ*, 871, 181
- Hasselquist, S., Zasowski, G., Feuillet, D. K., et al. 2020, arXiv e-prints, arXiv:2008.03603
- Hawkins, K., Jofré, P., Masseron, T., & Gilmore, G. 2015, *MNRAS*, 453, 758
- Hayden, M. R., Bovy, J., Holtzman, J. A., et al. 2015, *ApJ*, 808, 132
- Hayden, M. R., Holtzman, J. A., Bovy, J., et al. 2014, *AJ*, 147, 116
- Haywood, M. 2012, in European Physical Journal Web of Conferences, Vol. 19, European Physical Journal Web of Conferences, 05001
- Helmi, A., Babusiaux, C., Koppelman, H. H., et al. 2018, *Nature*, 563, 85
- Hill, V., Lecureur, A., Gómez, A., et al. 2011, *A&A*, 534, A80
- Hilmi, T., Minchev, I., Buck, T., et al. 2020, arXiv e-prints, arXiv:2003.05457
- Holtzman, J. A., Hasselquist, S., Shetrone, M., et al. 2018, *AJ*, 156, 125
- Horta, D., Schiavon, R. P., Mackereth, J. T., et al. 2021, *MNRAS*, 500, 1385
- Huertas-Company, M., Guo, Y., Ginzburg, O., et al. 2020, arXiv e-prints, arXiv:2006.14636
- Hunter, J. D. 2007, *Computing in Science and Engineering*, 9, 90
- Iorio, G. & Belokurov, V. 2019, *MNRAS*, 482, 3868
- Johnson, C. I., Rich, R. M., Kobayashi, C., et al. 2013, *ApJ*, 765, 157
- Jönsson, H., Holtzman, J. A., Allende Prieto, C., et al. 2020, arXiv e-prints, arXiv:2007.05537
- Kawata, D., Baba, J., Hunt, J. A. S., et al. 2020, arXiv e-prints, arXiv:2012.05890
- Kerber, L. O., Libralato, M., Souza, S. O., et al. 2019, *MNRAS*, 484, 5530
- Kerber, L. O., Nardiello, D., Ortolani, S., et al. 2018, *ApJ*, 853, 15
- Kunder, A., Koch, A., Rich, R. M., et al. 2012, *AJ*, 143, 57
- Kunder, A., Pérez-Villegas, A., Rich, R. M., et al. 2020, *AJ*, 159, 270
- Kunder, A., Rich, R. M., Koch, A., et al. 2016, *ApJ*, 821, L25
- Lagarde, N., Reylé, C., Robin, A. C., et al. 2019, *A&A*, 621, A24
- Laporte, C. F. P., Belokurov, V., Koposov, S. E., Smith, M. C., & Hill, V. 2020, *MNRAS*, 492, L61
- Leung, H. W. & Bovy, J. 2019, *MNRAS*, 483, 3255
- Li, Z.-Y. & Shen, J. 2012, *ApJ*, 757, L7
- Lian, J., Zasowski, G., Hasselquist, S., et al. 2020, *MNRAS*, 497, 3557
- Lindgren, L., Bastian, U., Biermann, M., et al. 2020, arXiv e-prints, arXiv:2012.01742
- Lucey, M., Hawkins, K., Ness, M., et al. 2021, *MNRAS*, 501, 5981
- Madore, B. F. 2016, *Astrophysics and Space Science Library*, Vol. 418, *Bulges: Seen from a Philosophically-Informed Historical Perspective*, ed. E. Laurikainen, R. Peletier, & D. Gadotti, 1
- Maiolino, R., Russell, H. R., Fabian, A. C., et al. 2017, *Nature*, 544, 202
- Majewski, S. R., Schiavon, R. P., Frinchaboy, P. M., et al. 2017, *AJ*, 154, 94
- Martig, M., Fouesneau, M., Rix, H.-W., et al. 2016a, *MNRAS*, 456, 3655
- Martig, M., Minchev, I., Ness, M., Fouesneau, M., & Rix, H.-W. 2016b, *ApJ*, 831, 139
- Masseron, T. & Gilmore, G. 2015, *MNRAS*, 453, 1855
- Matsunaga, N., Feast, M. W., Bono, G., et al. 2016, *MNRAS*, 462, 414
- Matteucci, F. 1991, in *Astronomical Society of the Pacific Conference Series*, Vol. 20, *Frontiers of Stellar Evolution*, ed. D. L. Lambert, 539
- Matteucci, F., Grisoni, V., Spitoni, E., et al. 2019, *MNRAS*, 487, 5363
- McWilliam, A. 1997, *ARA&A*, 35, 503
- McWilliam, A. & Rich, R. M. 1994, *ApJS*, 91, 749
- McWilliam, A., Wallerstein, G., & Mottini, M. 2013, *ApJ*, 778, 149
- McWilliam, A. & Zoccali, M. 2010, *ApJ*, 724, 1491
- Miglio, A., Chiappini, C., Mackereth, J. T., et al. 2021, *A&A*, 645, A85
- Minchev, I., Boily, C., Siebert, A., & Bienayme, O. 2010, *MNRAS*, 407, 2122
- Minchev, I., Chiappini, C., & Martig, M. 2013, *A&A*, 558, A9
- Minchev, I., Chiappini, C., & Martig, M. 2014, *A&A*, 572, A92
- Minchev, I., Nordhaus, J., & Quillen, A. C. 2007, *ApJ*, 664, L31
- Minniti, D. 1995, *AJ*, 109, 1663
- Minniti, D. 1996, *ApJ*, 459, 175
- Minniti, D., Lucas, P. W., Emerson, J. P., et al. 2010, *New A*, 15, 433
- Minniti, D., Olszewski, E. W., Liebert, J., et al. 1995, *MNRAS*, 277, 1293
- Minniti, D., Saito, R. K., Gonzalez, O. A., et al. 2014, *A&A*, 571, A91
- Minniti, D., White, S. D. M., Olszewski, E. W., & Hill, J. M. 1992, *ApJ*, 393, L47
- Miyamoto, M. & Nagai, R. 1975, *PASJ*, 27, 533
- Montalbán, J., Mackereth, J. T., Miglio, A., et al. 2021, *Nature Astronomy* [arXiv:2006.01783]
- Myeong, G. C., Vasiliev, E., Iorio, G., Evans, N. W., & Belokurov, V. 2019, *MNRAS*, 488, 1235
- Nandakumar, G., Schultheis, M., Hayden, M., et al. 2017, *A&A*, 606, A97
- Nataf, D. M., Udalski, A., Gould, A., Fouqué, P., & Stanek, K. Z. 2010, *ApJ*, 721, L28
- Navarro, J. F., Frenk, C. S., & White, S. D. M. 1997, *ApJ*, 490, 493
- Ness, M. 2012, in *Dynamics Meets Kinematic Tracers*, 9
- Ness, M. & Freeman, K. 2016, *PASA*, 33, e022
- Ness, M., Freeman, K., Athanassoula, E., et al. 2013a, *MNRAS*, 430, 836
- Ness, M., Freeman, K., Athanassoula, E., et al. 2013b, *MNRAS*, 432, 2092
- Ness, M., Zasowski, G., Johnson, J. A., et al. 2016, *ApJ*, 819, 2
- Nidever, D. L., Bovy, J., Bird, J. C., et al. 2014, *ApJ*, 796, 38
- Ortolani, S., Held, E. V., Nardiello, D., et al. 2019, *A&A*, 627, A145
- Pérez-Villegas, A., Portail, M., & Gerhard, O. 2017a, *MNRAS*, 464, L80
- Pérez-Villegas, A., Portail, M., Wegg, C., & Gerhard, O. 2017b, *ApJ*, 840, L2
- Pfenniger, D. 1984, *A&A*, 134, 373
- Pietrukowicz, P., Kozłowski, S., Skowron, J., et al. 2015, *ApJ*, 811, 113
- Poggio, E., Drimmel, R., Andrae, R., et al. 2020, *Nature Astronomy* [arXiv:1912.10471]
- Poggio, E., Drimmel, R., Cantat-Gaudin, T., et al. 2021, arXiv e-prints, arXiv:2103.01970
- Portail, M., Gerhard, O., Wegg, C., & Ness, M. 2017, *MNRAS*, 465, 1621
- Portail, M., Wegg, C., & Gerhard, O. 2015, *MNRAS*, 450, L66
- Price-Whelan, A. M., Sipőcz, B. M., Günther, H. M., et al. 2018, *AJ*, 156, 123
- Queiroz, A. B. A., Anders, F., Chiappini, C., et al. 2020, *A&A*, 638, A76
- Queiroz, A. B. A., Anders, F., Santiago, B. X., et al. 2018, *MNRAS* [arXiv:1710.09970]
- Queiroz, e. a. et al., in prep., *StarHorse distances and extinctions for spectroscopic releases and APOGEE DR16 selection effects*
- Rattenbury, N. J., Mao, S., Debattista, V. P., et al. 2007, *MNRAS*, 378, 1165
- Reid, M. J., McClintock, J. E., Steiner, J. F., et al. 2014, *ApJ*, 796, 2
- Rendle, B. M., Miglio, A., Chiappini, C., et al. 2019, *MNRAS*, 490, 4465
- Renzini, A., Gennaro, M., Zoccali, M., et al. 2018, *ApJ*, 863, 16
- Rich, R. M. 1988, *AJ*, 95, 828
- Rich, R. M., Origlia, L., & Valenti, E. 2012, *ApJ*, 746, 59
- Rich, R. M., Reitzel, D. B., Howard, C. D., & Zhao, H. 2007, *ApJ*, 658, L29
- Rojas-Arriagada, A., Recio-Blanco, A., de Laverny, P., et al. 2017, *A&A*, 601, A140
- Rojas-Arriagada, A., Recio-Blanco, A., Hill, V., et al. 2014, *A&A*, 569, A103
- Rojas-Arriagada, A., Zasowski, G., Schultheis, M., et al. 2020, *MNRAS*, 499, 1037
- Rojas-Arriagada, A., Zoccali, M., Schultheis, M., et al. 2019, *A&A*, 626, A16
- Romero-Gómez, M., Mateu, C., Aguilar, L., Figueras, F., & Castro-Ginard, A. 2019, *A&A*, 627, A150
- Rossi, L. J. 2015, *Astronomy and Computing*, 12, 11
- Saito, R. K., Hempel, M., Minniti, D., et al. 2012, *A&A*, 537, A107
- Sanders, J. L., Smith, L., & Evans, N. W. 2019a, *MNRAS*, 488, 4552
- Sanders, J. L., Smith, L., Evans, N. W., & Lucas, P. 2019b, *MNRAS*, 487, 5188
- Santiago, B. X., Brauer, D. E., Anders, F., et al. 2016, *A&A*, 585, A42

- Savino, A., Koch, A., Prudil, Z., Kunder, A., & Smolec, R. 2020, arXiv e-prints, arXiv:2006.12507
- Schönrich, R. & Binney, J. 2009, MNRAS, 399, 1145
- Schönrich, R., Binney, J., & Dehnen, W. 2010, MNRAS, 403, 1829
- Schultheis, M., Rich, R. M., Origlia, L., et al. 2019, A&A, 627, A152
- Schultheis, M., Rojas-Arriagada, A., García Pérez, A. E., et al. 2017, A&A, 600, A14
- Sharma, S., Hayden, M. R., & Bland-Hawthorn, J. 2020, arXiv e-prints, arXiv:2005.03646
- Smith, M. C., Evans, N. W., Belokurov, V., et al. 2009, MNRAS, 399, 1223
- Smith, R., Flynn, C., Candlish, G. N., Fellhauer, M., & Gibson, B. K. 2015, MNRAS, 448, 2934
- Spitoni, E., Verma, K., Silva Aguirre, V., et al. 2021, A&A, 647, A73
- Stebbins, J. & Whitford, A. E. 1947, ApJ, 106, 235
- Steinmetz, M., Guiglion, G., McMillan, P. J., et al. 2020, AJ in press, arXiv:2002.04512
- Surot, F., Valenti, E., Hidalgo, S. L., et al. 2019, A&A, 623, A168
- Tacchella, S., Carollo, C. M., Renzini, A., et al. 2015, Science, 348, 314
- Thorsbro, B., Ryde, N., Rich, R. M., et al. 2020, ApJ, 894, 26
- Vincenzo, F. & Kobayashi, C. 2020, MNRAS, 496, 80
- Virtanen, P., Gommers, R., Burovski, E., et al. 2019, scipyl/scipy: SciPy 1.2.1
- Wegg, C. & Gerhard, O. 2013, The Messenger, 154, 54
- Wegg, C., Gerhard, O., & Bieth, M. 2019, MNRAS, 485, 3296
- Wegg, C., Gerhard, O., & Portail, M. 2017, ApJ, 843, L5
- Weinberg, D. H., Holtzman, J. A., Hasselquist, S., et al. 2019, ApJ, 874, 102
- Wilson, J. C., Hearty, F., Skrutskie, M. F., et al. 2010, in Society of Photo-Optical Instrumentation Engineers (SPIE) Conference Series, Vol. 7735, Proc. SPIE, 77351C
- Wilson, J. C., Hearty, F. R., Skrutskie, M. F., et al. 2019, PASP, 131, 055001
- Wise, J. H., Turk, M. J., Norman, M. L., & Abel, T. 2012, ApJ, 745, 50
- Zasowski, G., Cohen, R. E., Chojnowski, S. D., et al. 2017, AJ, 154, 198
- Zasowski, G., Johnson, J. A., Frinchaboy, P. M., et al. 2013, AJ, 146, 81
- Zasowski, G., Schultheis, M., Hasselquist, S., et al. 2019, ApJ, 870, 138
- Zinn, J. C., Pinsonneault, M. H., Huber, D., & Stello, D. 2019, ApJ, 878, 136
- Zoccali, M., Gonzalez, O. A., Vazquez, S., et al. 2014, A&A, 562, A66
- Zoccali, M., Hill, V., Lecureur, A., et al. 2008, A&A, 486, 177
- Zoccali, M., Renzini, A., Ortolani, S., et al. 2003, A&A, 399, 931
- Zoccali, M., Vazquez, S., Gonzalez, O. A., et al. 2017, A&A, 599, A12
- ¹ Leibniz-Institut für Astrophysik Potsdam (AIP), An der Sternwarte 16, 14482 Potsdam, Germany
e-mail: aqueiroz@aip.de
- ² Laboratório Interinstitucional de e-Astronomia - LIneA, Rua Gal. José Cristino 77, Rio de Janeiro, RJ - 20921-400, Brazil
- ³ Department of Astronomy, Universidade de São Paulo, São Paulo 05508-090, Brazil
- ⁴ Instituto de Astronomía, Universidad Nacional Autónoma de México, A. P. 106, C.P. 22800, Ensenada, B. C., México
- ⁵ Institut de Ciències del Cosmos, Universitat de Barcelona (IEEC-UB), Carrer Martí i Franquès 1, 08028 Barcelona, Spain
- ⁶ Instituto de Física, Universidade Federal do Rio Grande do Sul, Caixa Postal 15051, Porto Alegre, RS - 91501-970, Brazil
- ⁷ University of Arizona, Tucson, AZ 85719, USA
- ⁸ Observatório Nacional, Sao Cristóvão, Rio de Janeiro, Brazil
- ⁹ Observatoire de la Côte d'Azur, Laboratoire Lagrange, 06304 Nice Cedex 4, France
- ¹⁰ Department of Astronomy, University of Virginia, Charlottesville, VA 22904-4325, USA
- ¹¹ Instituto de Astrofísica, Pontificia Universidad Católica de Chile, Av. Vicuña Mackenna 4860, 782-0436 Macul, Santiago, Chile
- ¹² The Carnegie Observatories, 813 Santa Barbara Street, Pasadena, CA 91101, USA
- ¹³ Departamento de Astronomía, Universidad de Concepción, Casilla 160-C, Concepción, Chile
- ¹⁴ Instituto de Astronomía y Ciencias Planetarias de Atacama, Universidad de Atacama, Copayapu 485, Copiapó, Chile
- ¹⁵ Instituto de Astronomía, Universidad Católica del Norte, Av. Angamos 0610, Antofagasta, Chile
- ¹⁶ Instituto de Astrofísica de Canarias (IAC), E-38205 La Laguna, Tenerife, Spain
- ¹⁷ Universidad de La Laguna (ULL), Departamento de Astrofísica, E-38206 La Laguna, Tenerife, Spain
- ¹⁸ Instituto de Investigación Multidisciplinario en Ciencia y Tecnología, Universidad de La Serena. Avenida Raúl Bitrán S/N, La Serena, Chile
- ¹⁹ Departamento de Física, Facultad de Ciencias, Universidad de La Serena, Cisternas 1200, La Serena, Chile
- ²⁰ Department of Physics & Astronomy, University of Utah, Salt Lake City, UT, 84112, USA
- ²¹ NSF Astronomy and Astrophysics Postdoctoral Fellow
- ²² Centro de Astronomía (CITEVA), Universidad de Antofagasta, Avenida Angamos 601, Antofagasta 1270300, Chile
- ²³ National Optical Astronomy Observatories, Tucson, AZ 85719, USA

Appendix A: Probabilities of flipping the velocity

Here we show if the errors in velocity would produce inconsistent results in our analysis, especially the case where the errors can cause the measured parameter to flip their original sign. This situation could fabricate the counter-rotating bump we observe in Section 7.1.

To prove this is not the case in our data, we performed 1000 Monte Carlo realizations, considering the errors in the distance, the line-of-sight velocity, and the proper motions to calculate the star's flipping velocity probability. The parameter that most influences the error in velocities is the distance. Figure A.1 shows the median velocity component against Galactocentric distance colour coded by the probability of flipping the sign. As can be seen in the Figure, this probability is higher for small velocities, in the case of $V_\phi < -50$ km/s. For V_ϕ we have that 61% of the stars in the RPM sample will never change sign, from the $\sim 8\,000$ stars $\sim 1\,000$ have more than 50% probability of changing direction. If we split the stars with $> 50\%$ of changing the sign in positive and negative, we have 559 ($\sim 7\%$) that goes from positive to negative and 458 ($\sim 6\%$) that goes from positive to negative. This shows that the errors in V_ϕ are symmetric and would not likely produce the extended tail in velocities < -50 km/s we see in Section 7.1. The flipping probabilities are also symmetric in the other components of the velocity, as one can notice from Figure A.1.

Appendix B: Orbits comparison

Here we show the differences in the orbital parameters if they were calculated with different pattern speeds for the bar potential. We have checked that using a different pattern speed does not bring any inconsistency in the presented results; Figure B.1 shows the relative errors between eccentricity, $|Z|_{max}$, pericentre and apocentre for two different pattern speeds of 35 and 50. The relative errors are generally not higher than 25%. Errors are more significant for low eccentricity stars and pericenters determination.

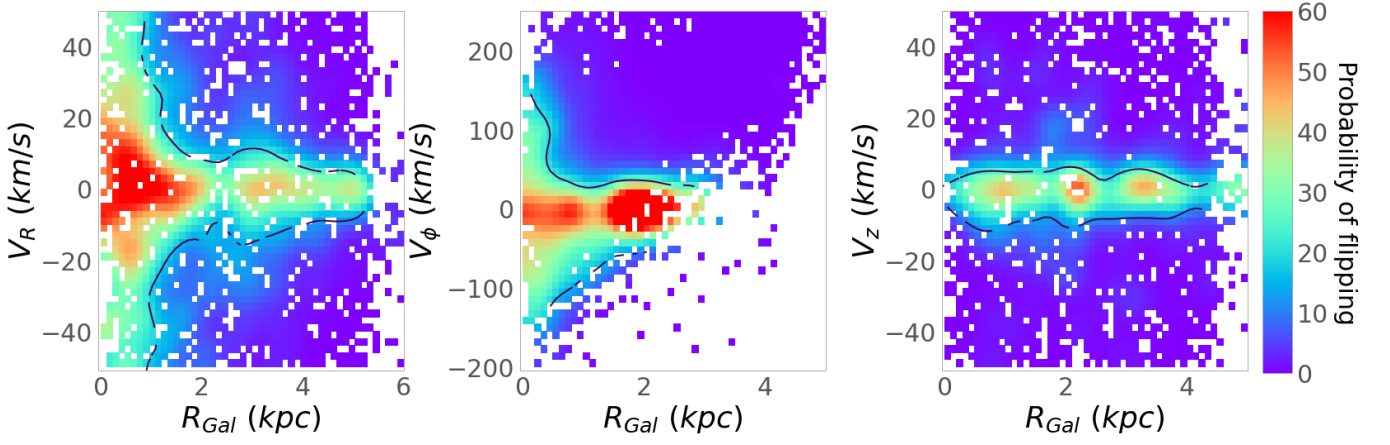


Fig. A.1. From left to right: Radial, azimuthal and vertical velocities against Galactocentric radius. The diagrams are colour coded by the velocity flipping sign probability.

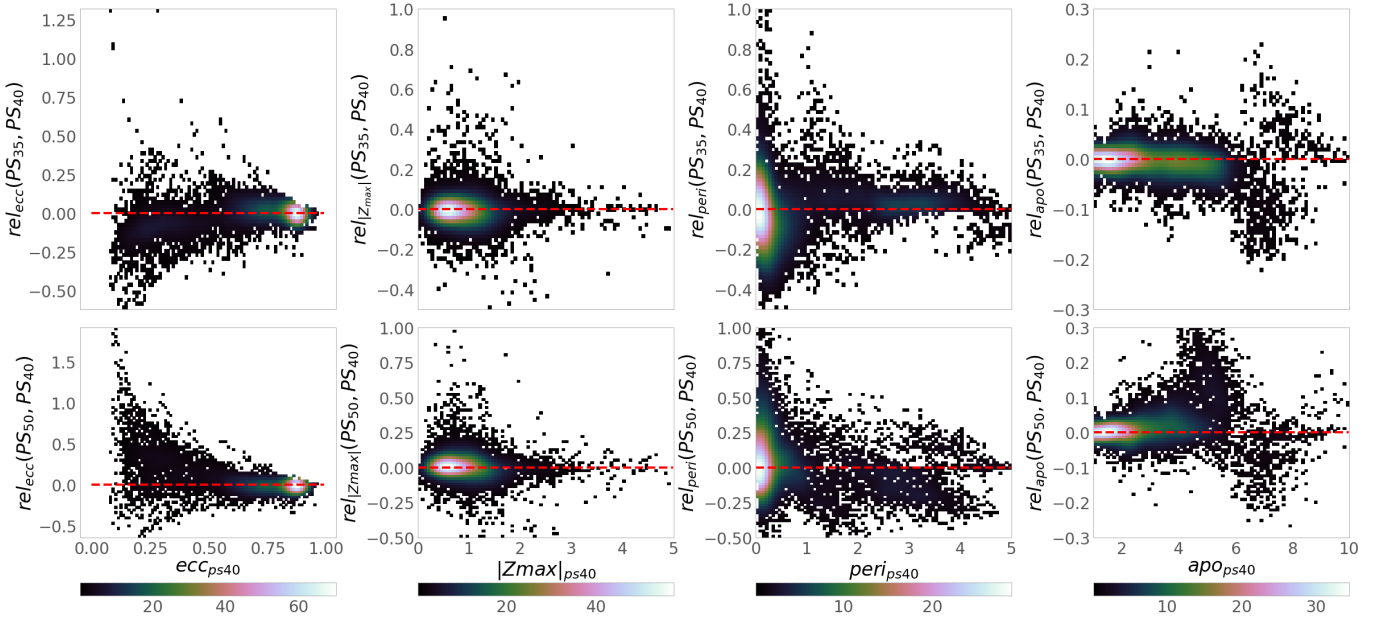


Fig. B.1. Comparison between orbits with the same bar potential but with varying pattern speeds. From left to right relative errors for eccentricity, Z_{\max} , pericentre, apocentre. The upper panels compare pattern speeds of 40 and 35; lower panels pattern speeds 40 and 50.